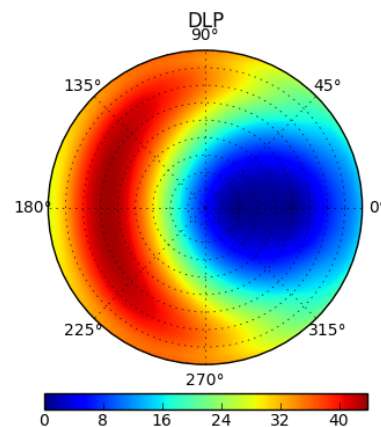# Validation and Application of SCIATRAN polarisation simulations for ground-based multi-axis DOAS measurements

Master Thesis

Author: Andrés Bernal S.
Enrollment number: 2991892

Examiner 1: Prof. Dr. J.P. Burrows
Examiner 2: Dr. Marco Vountas

Institute of Environmental Physics and Remote Sensing (IUP)
Postgraduate Programme Environmental Physics (PEP)
University of Bremen

Bremen, 29 December 2017

Universität Bremen*

.

Contents

1 Abstract

The polarisation of light, and the physics behind it, is a topic which has been studied for many years. For atmospheric research, polarisation has been investigated by the use of experiments, computer models, or a combination of them, and the obtained information has broadened our knowledge about different topics such as aerosols, clouds, or trace gas distributions. In this master thesis, the validation and application of SCIATRAN polarisation simulations for a ground-based MAX-DOAS instrument are described. The thesis starts with a theoretical background about polarisation processes in the atmosphere, on land and in the water, followed by a description of the two techniques used in this thesis: the Differential Optical Absorption Spectroscopy (DOAS) and the Multi-Axis DOAS (MAX-DOAS).

The existing MAX-DOAS instrument at the University of Bremen was adapted to perform polarized measurements, which was done by including a computer controlled polarizer in the instrument. For one month, automatic measurements were performed with this set-up, and data for selected days with clear conditions were analysed. SCIATRAN simulations with polarisation were performed for ground-based geometry covering different wavelengths, multiple aerosol scenarios, and different solar zenit angles. In general, a good agreement was found between the SCIATRAN polarisation simulations and the observed experimental data radiance (intensity), which was used to estimate the Stokes parameters (I, Q, U) along with the degree of linear polarisation (DLP).

2 Acknowledgements

Foremost, I would like to thank the University of Bremen and the Program for Environmental Physics (PEP) to give me the opportunity to become a master student. I am also thankful to Prof. Dr. John Burrows and Dr. Marco Vountas for accepting to be my thesis reviewers. Thanks for the comments at the first stage of this process.

I would like to express my gratitude to Dr. Andreas Richter for granting me the opportunity to do my thesis in his group (DOAS) and for his support during all stages of the research presented here. His comments, patience and scientific insight, but also his practical help during the setting up of the experiment with a polarizer, were of great help.

I am thankful to all the people, Karolin kornehl, Dr. Hella van Asperen, Dr. Leonardo Alvarado, Dr. Sebastian Montealegre, Midhun George, who helped me with the corrections, comments and suggestions for the final document, thank you so much for your time and understanding. Special thanks to the families Samacá Barragan and Bernal Samacá.

At last, I would like to thank my friends for supporting me during this master degree.

3 Introduction

Motivation

In the last decades, polarisation of light has been studied to investigate how it can be used to retrieve information about atmospheric components, such as aerosols or clouds, which are known to affect the Earth's climate. To utilize this information, a radiative transfer model, which includes polarisation effects, can be used to understand how the solar energy is reflected, scattered, absorbed and transmitted when it reaches the Earth's atmosphere and how polarisation is changed during these processes.

However, studying polarisation in the atmosphere is challenging due to the vast amount of particles present in the air. Their impact on atmospheric polarisation depends on their size distribution and shape. Not all particles are spherical and they are usually randomly oriented, wherefore the degree of polarisation varies largely (Bohren and Clothiaux, 2006). Therefore, by the use of a radiative transfer model such as SCIATRAN (Rozanov et al., 2014), the shape and the size of the particles can be used to estimate polarisation effects for given aerosols, wavelengths or parameters, which will be explained later in this chapter.

The measurement of atmospheric polarisation is being used for two main applications; one is related to the study of aerosols, and the second one is related to the development of computer models, which are being used to understand the scattering properties of the atmosphere. The first application is used for improving the remote sensing of aerosols and clouds (Emde et al., 2010), as well as for studying the sensitivity of polarisation to different types of particles. Different particles show different polarisation characteristics, especially at shorter wavelengths such as the UV range. Thus, studying polarisation is essential to understand the scattering of sunlight in a pure atmosphere and can also be used to retrieve information on the type and the shape of different aerosols (Stamnes and Stamnes, 2015).

The second application concerns the modelling of atmospheric radiation, and considers the polarisation caused by particles and molecules. For the accurate modelling of radiative transfer, these effects have to be considered. The measured polarisation can be used to assess the accuracy of a radiative transfer model.

As a property of light, polarisation is interesting by itself, and its measurements can be applied to different fields of research. For instance, polarisation is used in biology research in order to learn how some animals can perceive polarisation and how they use it to orientate themselves (Horváth and Varjú, 2004). Furthermore, its measurements can also be employed to design new devices to measure polarisation in the atmosphere. For example, the measurement of polarized sunlight is being used to identify atmospheric aerosols and to study their properties.

An approach to measure polarisation in the atmosphere is by the use of spectroscopic methods, which allow the collection of information about atmospheric gas concentrations. Thus, by using polarisation measurements, a method such as Multi-Axis-Differential Optical Absorption Spectroscopy (MAX-DOAS) is able to provide information about gas concentration and gas distribution in the atmosphere (Hasekamp and Landgraf, 2002) with minor errors in the retrieval information of the distributed trace gases.

Solar scatter intensity in the atmosphere has been studied intensively, since quantifying the variation in intensity, it is possible to obtain explanations, among others, for phenomena such as blue skies and rainbows (refraction and internal reflection in water drops), wherein the direction of polarisation is a critical factor (Können, 1987). Another important example of how polarisation is used for research, is the development of a radiative transfer model which aims at understanding how the intensity and polarisation of light is diffusely transmitted through the atmosphere, thereby considering homogeneous particles and a plane-parallel atmosphere, where the polarized light is described by the Stokes components (Chandrasekhar and Elbert, 1954).

However, this model is not totally accurate with respect to the reality, since a clear sky without any cloud interference is assumed (Tousey and Hulburt, 1947). Also, only under some assumptions can the Earth's atmosphere be considered to be plane parallel. Under those conditions, the solution of the radiative transfer equations given by Chandrasekahr are valid, and therefore, the polarisation of the scattered light yield functions as a good indicator for the scattering processes (Sekera, 1957).

As the amount of study on polarisation in the atmosphere was expanding, additional parameters such as wavelength range, aerosol optical thickness, refractive index, and other atmospheric parameters were investigated throughout different experiments. The radiative transfer model was also modified according to these new findings, as well as to different concepts such as to a spherical atmosphere, to multiple scattering, or to the presence of inhomogeneous particles. Moreover, polarisation has also been used to detect particle properties, to study the composition of clouds, as well as to investigate the turbidity of the atmosphere (Hansen and Hovenier, 1974). Furthermore, polarisation has been employed to study the type, form, and kind of particles present in the atmosphere or clouds (Liou, 2002).

Particles, such as aerosols, molecules, water droplets or ice crystal, are responsible for the polarisation of scattered sunlight. Moreover, in the case of aerosols, they have a significant impact on the Earth's climate and the formation of clouds (Emde et al., 2010). Therefore, measurements of polarisation can be used to improve the remote sensing of these atmospheric components as well as to collect information on their optical and microphysical properties. For these reasons, models that include

polarisation and other variables are essential to be able to interpret and analyze measurements or simulations of polarisation. Some of the models which can be used for these purposes are: SCIATRAN, 3DMCPOL, IPOL, MYSTIC, Pstart, SHDOM, and SPARTA (Emde et al., 2015). Polarisation data of sky-light can be collected by satellite, aircraft or ground based measurements. With this collected data it is possible to study the vertical distribution of the trace gases in the atmosphere. A method to estimate their vertical distribution is by studying the intensity as well as the wavelength dependency of the polarisation, as described in (Hasekamp and Landgraf, 2002).

The main focus of this master thesis is to asses the comparability of SCIATRAN with MAX-DOAS measurements for certain test cases, in order to see how reliable the program is when polarisation simulations are done. To validate SCIATRAN polarisation simulations, it is necessary to compare the modeled radiances with ground-based observations. For this thesis, measurements were performed with a Multi-Axis DOAS instrument, which was operated on clear sky days. The following objectives for this thesis were defined: 1) Assembling a suitable optical set-up to enable the MAX-DOAS instrument to perform polarization sensitive measurements, 2) taking a series of measurements on clear days, 3) running SCIATRAN for the appropriate scenarios, and comparing the results with the measurements.

The thesis work begins with a general description of polarisation, followed by an explanation about its importance and its effects in the atmosphere (Chapter 4, Sections 4.1-4.4). The three subsequent sections (Sections 4.5-4.8) explain the scattering processes related to polarisation. In Section 4.9, a radiative transfer balance is explained, which takes polarisation effects into account. The following section (Section 4.10) discusses SCIATRAN, including a description of the parameters used in the thesis work. Chapter 5 deals with the DOAS method, the Air Mass Factors (AMF), and the Multi-Axis DOAS. Finally, at the end of Chapter 5, a short explanation of DOAS and polarisation is given, as well as a description of the setup used for the thesis work.

In Chapter 6, the results are shown for the different goals of the thesis work. The first part concerns the reproduction and comparison of simulations according to the study of (Emde et al., 2010). Also, additional new simulations for other solar zenith angles and aerosol scenarios are presented. Then, a description of the data acquisition of the experiment is given, as well as plots and comparisons between the experiment and the simulated data are shown. Section 6.15 deals with polarisation and its changes for the ultraviolet (UV) and the visible (vis) spectrum. Then, a discussion of the results can be found in Chapter 7, followed by conclusions and a summary of the thesis work in Chapter 8.
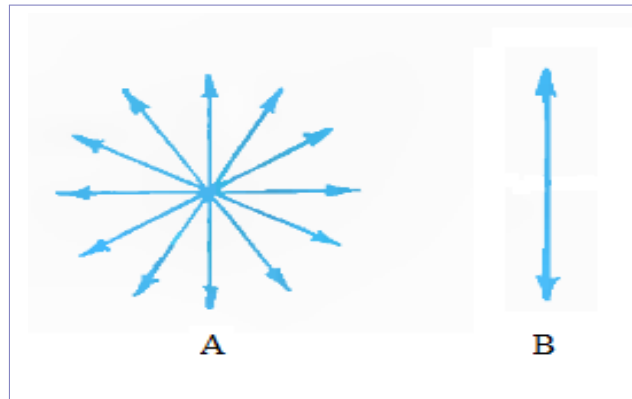
Figure 1: Polarisation of light, A) represent unpolarized light in several directions. B) Represent polarized light

4 Scientific background

4.1 Polarisation

The nature of light is characterized by having as well an electric as a magnetic field, the two fields being oriented orthogonally, and oscillating perpendicularly to the direction of propagation. Light can oscillate in many planes and if there is no preferred direction, it is called unpolarized light. However, when light vibrates in only one plane, as shown in Figure 1, it is named polarised light (Können and Beerling, 1985).

Polarisation of light is produced by the interaction between an electromagnetic wave and an object. The object scatters part of the incoming light, but also absorbs part of the incoming light. If the light is absorbed by a dipole, the emitted photons are polarized in the plane in which the electrons are oscillating (Band, 2006).

Polarisation of light can be linear, circular and elliptical, as well as a combination of linear and circular polarisation. For example, linear polarisation can be created by Rayleigh scattering of sunlight on air molecules. Circular polarisation is rare in nature but can occur through the conversion of linear polarised light into circularly polarised light by reflection. Circular polarisation is characterized by the sense of rotation i.e. counter-clockwise or clockwise motion. As a property of light, the state of polarisation is described by the Stokes vector S(I,Q,U,V), where the first three components are related to linear polarisation and the last one to circular polarisation. I represents the intensity, Q and U describe the linear polarisation, and V is associated with the circular polarisation (Stamnes and Stamnes, 2015).
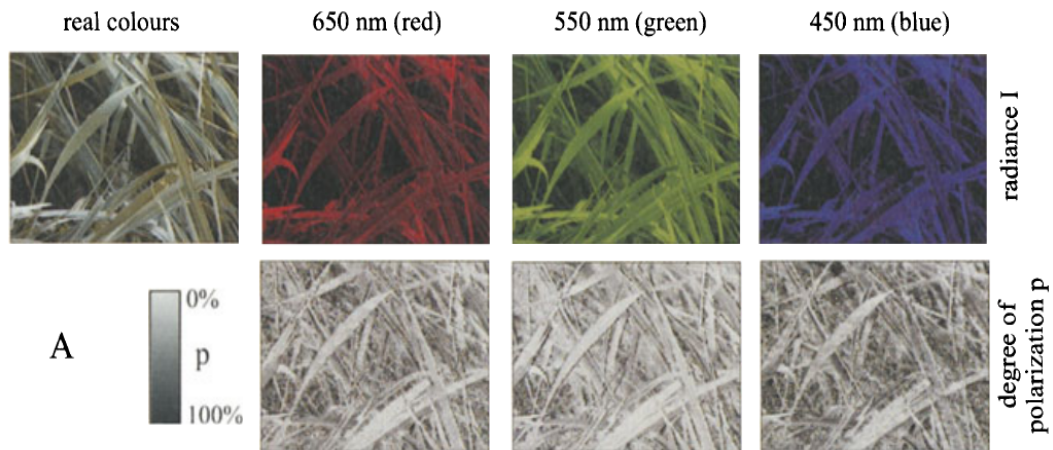
Figure 2: A) Variation of the degree of polarisation and color in grass leaves (Horváth and Varjú, 2004)

4.2 Polarisation in the Earth-atmosphere system

Polarisation of UV and vis sky-light in the Earth-atmosphere system is produced by scattering and reflection of sunlight in the atmosphere and on the ground. Due to the number of atmospheric components, sunlight can be scattered more than once, yielding multiple scattering. Furthermore, depending on the size of the suspended particles or molecules with respect to the considered wavelength in the atmosphere, scattering can be classified as Rayleigh scattering or as Mie scattering. The former occurs when particles such as molecules are smaller than the wavelength of the incoming sunlight, the latter happens for particles larger than the wavelength. Thus, by analyzing the scattered light and its polarisation, it is possible to retrieve information about the physical properties of the planetary atmospheres (Hansen and Hovenier, 1974).

4.3 Polarisation for solid surfaces/on the ground

Polarisation on a flat surface is created by the interaction of light with an interface, e.g. air or glass. The interface affects the trajectory of the outgoing light. Part of the incident light is refracted and another part is reflected. When the angle between the incident and the reflected light is 90°, the reflected light is completely polarized. This angle is called the Brewster's angle or polarisation angle, which can be derived from Snell's Law (Kokhanovsky, 2008).

Polarisation, as induced by light interacting with a surface, depends on the way how the plain is illuminated. As previously described, over a flat surface, the polarisation is created by reflection. For the Earth's surface, grass, snow, sand-plains and other type of land covers create strong polarisation at 90° with respect to the Sun,

but the polarisation depends on the reflective capacity, which means dark surfaces produce stronger polarisation than bright ones, which is called the *Umov* effect. In the case of vegetation, depending on the orientation of their blades, leaves can cause polarisation, as is shown in Figure 2 (Können and Beerling, 1985; Horváth and Varjú, 2004).

By use of polarisation observations on land, it is possible to characterize vegetation cover. However, because of different factors such as multiple scattering from rough surfaces, models and parameter conditions are hard to define, and a geometrical characterization of the surface is needed to improve data quality of polarisation measurements (Curran, 1982; Kozlov, A.I. et al., 2004).

4.4   Polarisation in water

Under water, unpolarized sunlight can be partially elliptically polarized by scattering on suspended living and inert matter. In accordance with the size of the living organisms, Rayleigh scattering can for instance take place on a virus, while in the case of phytoplankton, Mie scattering is predominant as phytoplankton tends to be larger than visible wavelengths (Martin, 2004; Kokhanovsky, 2004).

Using the elliptical polarisation, it is feasible to study microphysical characteristics of ocean water. However, the effect of chiral biological particles in water needs to be take into account, as these particles can rotate the plane of the polarisation from the incident polarized light (Kokhanovsky, 2004).

Furthermore, by measuring the intensity, the frequency and the polarisation of the reflected or emitted radiation from the ocean surface, it is possible to estimate variables such as surface temperature, salinity, wind speed and direction as well as the degree of ice coverage (Martin, 2004).

4.5   Scattering in the atmosphere

Unpolarized sunlight entering the atmosphere can be scattered by water droplets, molecules, ice particles or aerosols. These substances scatter, and thereby change the light intensity and its (angular) polarisation (gates., 1980). The scattering can be elastic or inelastic, and it depends on the size of the particle and the vibration states of the molecule. Elastic scattering occurs when there is a change of the energy of the photon and, during this type of scattering, only the direction of the photons is changed (Platt and Stutz, 2008). The ratio between the size of the particle and the wavelength of the incident radiation defines the kind of scattering. Elastic scattering in the atmosphere can be Rayleigh or Mie scattering, while inelastic scattering is known as Raman scattering. Raman scattering can occur as rotational Raman scattering on air molecules or as vibrational Raman scattering in ocean water (Vountas, et all, 2003). For the scattering processes in the atmosphere, there is a general
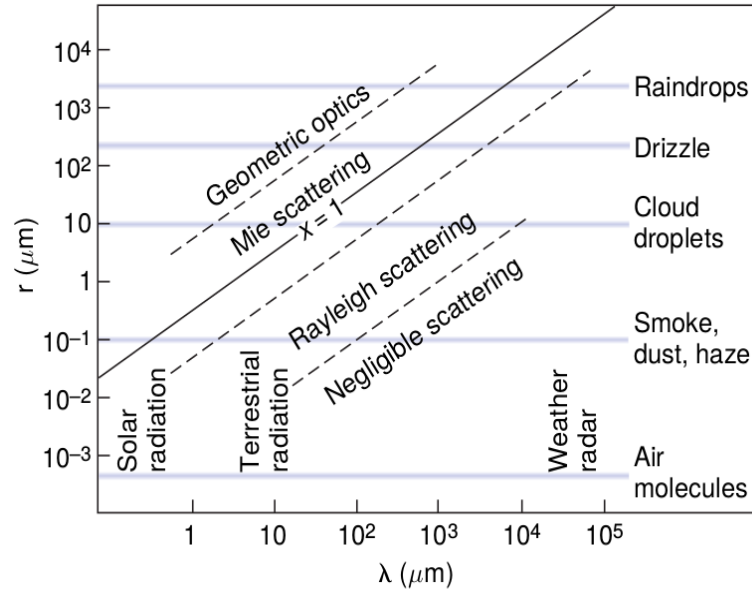
Figure 3: Size parameter x as a function of lambda and radius of the object (Wallace and Hobbs, 2006)

expression for the scattered intensity as a function of the initial intensity (I_0), the scattering cross-section (σ), the radius (r) of the scattered sphere, and the phase function P(θ) which is given by:

$$I = I_0 \frac{\sigma P(\theta)}{4\pi r^2} \tag{1}$$

4.6 Rayleigh scattering

A clear sky is cloudless and only composed of aerosols and air molecules which display variations in air density. These variations and particles scatter light because they are small compared to the wavelength of sunlight. The scattering efficiency is inversely proportional to the fourth power of the wavelength. By this process, the blue wavelengths of incoming solar radiation are scattered much more than the red wavelengths, resulting in the blue color of cloudless sky. A way to study the type of scattering, is by quantifying the parameter x, which can be described as:

$$x = \frac{2\pi r}{\lambda} \tag{2}$$

where r is the radius of the particle and λ the incident wavelength. Therefore, for x $\ll$ 1, Rayleigh scattering takes place, as is shown in Figure 3.
Rayleigh scattering explains how the intensity of incoming light tends to change due to the interaction between electromagnetic waves and the particles that compose a given substance. In Rayleigh scattering, the variation of intensity depends on

four parameters: the wavelength λ of the incoming light, the polarizability α of the molecule, the scattering angle θ, and the distance r between the molecule and the detection point of intensity given by (Liou, 2002):

$$I = \frac{I_0}{r^2}\alpha^2 \left(\frac{2\pi}{\lambda}\right)^4 \frac{1 + cos^2\theta}{2} \tag{3}$$

In addition to the different parameters that describe Rayleigh scattering, there are some external factors that are related with Rayleigh scattering, such as the cross section σ and the phase function $P(\theta)$. The cross section describes the amount of energy of the incoming light that, after interaction with a particle, is distributed isotropically over the area of a sphere of radius r, and whose center is the scatterer point, and for Rayleigh scattering is given by:

$$\sigma = \frac{8\pi^3(m^2 - 1)^2}{3\lambda^4 N_s^2}f(\delta) \tag{4}$$

where m is the refractive index of the molecules, Ns is the total number of molecules per unit volume, and $f(\delta)$ is a correction factor for the anisotropy of the molecules (Liou, 2002).

The phase function $P(\theta)$ describes the angular distribution of the scattered intensity, which for Rayleigh scattering is uniformly distributed in forward and backward directions:

$$P(\theta) = \frac{3}{4}(1 + cos^2\theta) \tag{5}$$

wherein $P(\theta)$ is maximum in the forward direction ($\theta=0°$) but also in the backward direction ($\theta=180°$), as is shown in Figure 4.
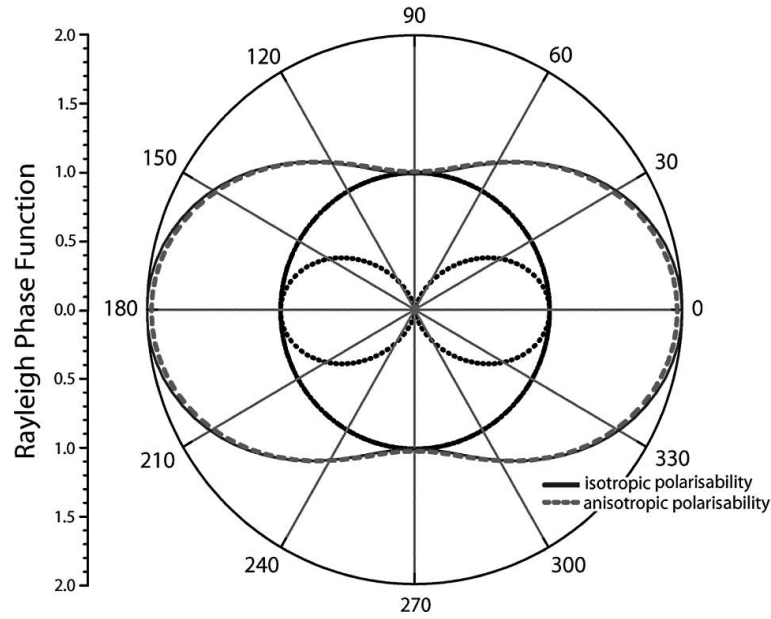
Figure 4: Rayleigh scattering phase function P(θ) (Platt and Stutz, 2008)

Therefore, at forward and backward directions, scattered sunlight is unpolarized (Platt and Stutz, 2008). However, scattered light at other angles is partially polarized, and is totally polarized at 90° when the scattered light is perpendicular to the incident light (Salby and Dmowska, 1996). Thus, after Rayleigh scattering, the degree of linear polarization (DLP) is:

$$DLP = -\frac{cos^2\theta - 1}{cos^2\theta + 1} \tag{6}$$

The DLP is not only determined by the scattering angle, since there are other factors that affect it as well. Among them one can count aerosols, whose geometrical form allows the light to scatter in several ways. Also, molecules can have a linear or a spherical symmetry, and are therefore oriented in many different directions, which can cause a reduction in the polarisation effects of sunlight. Thus, only molecules with a direction perpendicular to the incoming solar light can achieve 100% of DLP.

Another fact that impacts the DLP, in accordance to the Rayleigh scattering, is the assumption that only single scattering occurs in the atmosphere. However, due to the myriad of particles in the atmosphere, there is multiple scattering of light. For instance, in the case of superposition of two or more beams, there is no production of total polarisation of sunlight at 90° because of their different states of polarisation (Bohren and Clothiaux, 2006). An example of the degree of polarisation for sunlight scattered by a spherically symmetric dipole is illustrated by Figure 5.
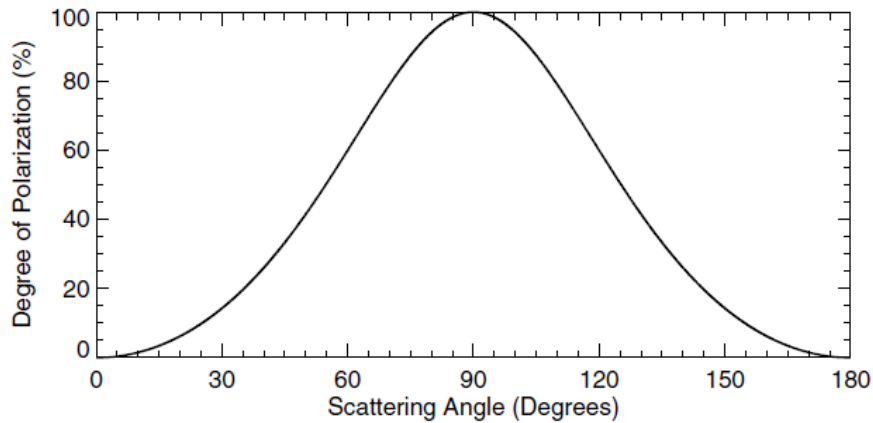
Figure 5: Degree of linear polarisation as a function of the scattering angle for Rayleigh scattering (Bohren and Clothiaux, 2006)

4.7 Mie scattering

Another type of scattering in the atmosphere takes place when the size of the particles is similar or larger than the incident wavelength. In that situation, and as shown in Figure 3, the size parameter is $x \gtrsim 1$, and the process is called Mie scattering. Mie scattering explains the interaction between a plane wave and an homogeneous and symmetric particle. Its most known effect is the whitish appereance of the sky as well as the white color of clouds (Wallace J, 2006) (Salby and Dmowska, 1996).

The change of intensity in the case of Mie scattering, can be studied from a general expression, which is valid for molecules and particles larger than the incident wavelength, and is given in equation 1 (Liou, 2002), and again here:

$$I = I_0 \frac{\sigma P(\theta)}{4\pi r^2} \qquad (7)$$

where I_0 is the initial intensity, $P(\theta)$ is the phase function, r is the distance between the interaction and the point of detection of intensity, 4π corresponds to the solid angle, and σ is the cross-section. In the case of Mie scattering, the scattering cross-section can be approximated by:

$$\sigma(\lambda) = (Q\pi R^2) \qquad (8)$$

with Q as the scattering efficiency and R as the radius of the particle. r is related with the size parameter and Q can be estimated by an expansion equation taking into account the polarisability of the particles. For non-spherical particles, the treatment of Mie scattering can be given by an analytical approximation using the Henyey-Greenstein phase function. However, in connection to Rayleigh scattering, the cross-section in Mie scattering can also be approximated by (Platt and Stutz, 2008):
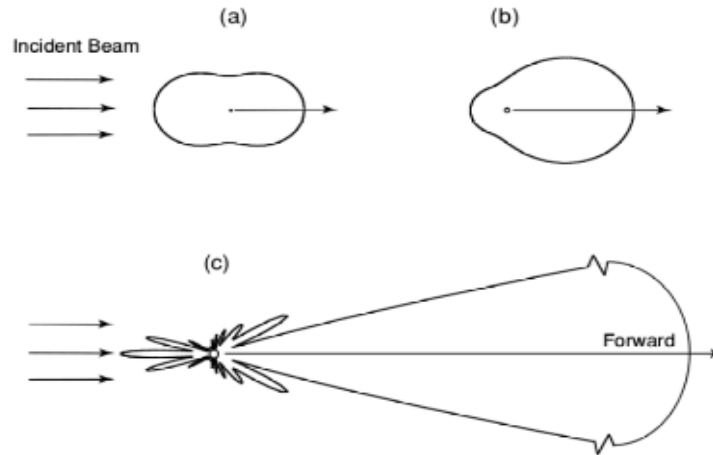
Figure 6: Angular patterns of the scattered intensity from spherical aerosols of a) $10^{-4}\mu$m, (b) 0.1 μm, and (c) 1 μm sizes illuminated by visible light (Liou, 2002).

$$\sigma(\lambda) \sim p(\lambda)^{-\alpha} \qquad (9)$$

where α is the Ångström exponent. In the case of the atmosphere, Mie scattering for symmetric and uniform particles, with a size similar to the incident wavelength, is produced by clouds particles, aerosols, small water droplets and other suspended particles. The scattering angular patterns for different sizes of aerosols and incident wavelength range are displayed in Figure 6.

In contrast to the Rayleigh scattering phase function, which is shown in Figure 4, the distribution of Mie scattered radiation is dominated by a peak in the forward direction and is stronger for larger particles.

4.8   Raman scattering

Another case of scattering, which takes place in the atmosphere as well as in the ocean (or other natural waters), is Raman scattering. The interaction of sunlight and a molecule in the air or ocean can produce two effects in the energy of the molecule: it can either gain or loose energy when the interaction takes place, resulting in a change in the frequency of the scattered photon. Hence, Raman scattering is considered inelastic scattering due to the shift of states of excitation of the molecule during the scattering process (Band, 2006; Platt and Stutz, 2008).

The scattering particle (molecule) changes its state of excitation by internal energy transitions, either rotational or vibrational. For vibrational Raman scattering, changes in the state of excitation are small and its effects in the atmosphere are

weaker. However, in the ocean vibrational Raman scattering can play an important role (Platt and Stutz, 2008; Vountas et al., 2003). Vibrational Raman scattering modifies the spectrum of light in the deep ocean, producing more yellow and red radiation (Jonasz and Fournier, 2007).

In the case of rotational Raman scattering, its effects in the atmosphere are not as weak as for the vibrational Raman scattering. By this rotational Raman scattering, the intensity of the photons after interaction with atmospheric molecules is distributed in a wide range of nanometers (Burrows et al., 2011). Another effect of rotational Raman scattering yields the Ring effect, a phenomenon that results in a filling-in of the solar Fraunhofer lines making them smaller compared to direct sunlight observations (Vountas et al., 1998).

Regarding to polarisation of light in the atmosphere, in respect to rotational Raman scattering the intensity of sunlight can be reduced, yielding a decrease of the degree of polarisation. Additionally, polarisation effects of light in the atmosphere can be described by the isotropic and anisotropic components of Raman scattering (Platt and Stutz, 2008; Landgraf et al., 2004).

4.9   The radiative transfer equation (RTE)

The radiative transfer equation describes how radiation changes due to the electro-magnetic interaction with matter, as well as the different processes that occur during the interaction. There are several RTE models existing, which individual suitabilitiy is depending on the geometry of the atmosphere, the type of particles considered, and the treatment of single and multiple scattering (Bohren and Clothiaux, 2006; Stamnes and Stamnes, 2015; Liou, 2002). However, a general case of RTE can be described as follows. For absorption and emission phenomena in the atmosphere, the radiative transfer equation according to (Rozanov et al., 2014) is given by:

$$\frac{dI(\lambda)}{ds} = -I(\lambda)\epsilon(\lambda) + \epsilon(\lambda)B(\lambda) \tag{10}$$

where the left hand side of the equation represents the change of intensity along a path ds. The first term on the right hand side is the attenuation due to absorption and scattering effects. The second term describes the gain due to scattering. $\epsilon(\lambda)$ is called the extinction coefficient and represents the sum of absorption and scattering coefficients, while B(λ) represents the source function.

If the effect of polarisation is included, the scalar intensity is replaced by the Stokes vector. The radiative transfer equation in terms of the optical depth τ, the cosine of the scattering angle u, and the zenith angle ϕ for the direction of propagation, can be written as:

$$u\frac{d\mathbf{I}}{d\tau} = \mathbf{I}(\tau, u, \phi) - \mathbf{S}(\tau, u, \phi) \tag{11}$$

where $\mathbf{I}(\tau,\mathrm{u},\phi) = [I, Q, U, V]^T$ represent the Stokes vector, and T notifies the transpose operation (Jackson, 1975). The total intensiy $\mathbf{I}$ is given by:

$$I^2 = Q^2 + U^2 + V^2 \tag{12}$$

I, Q, U and V are called the Stokes parameters and they are defined with respect to a certain reference plane. I represent the intensity, Q and U describe the linear polarisation and V is associated with the circular polarisation. V can be ignored for scattering by the Earth's atmosphere and for reflection by the Earth's surface. $\mathbf{S}(\tau,\mathrm{u},\phi)$ is the source function in the vector case (Stamnes and Stamnes, 2015; Tilstra et al., 2014).

As I, Q, U describe linear polarisation, they are related with the degree of linear polarisation given in equation (6). In that way, the DLP in function of these Stokes parameters becomes:

$$DLP = \frac{\sqrt{Q^2 + U^2}}{I} \tag{13}$$

4.10 SCIATRAN
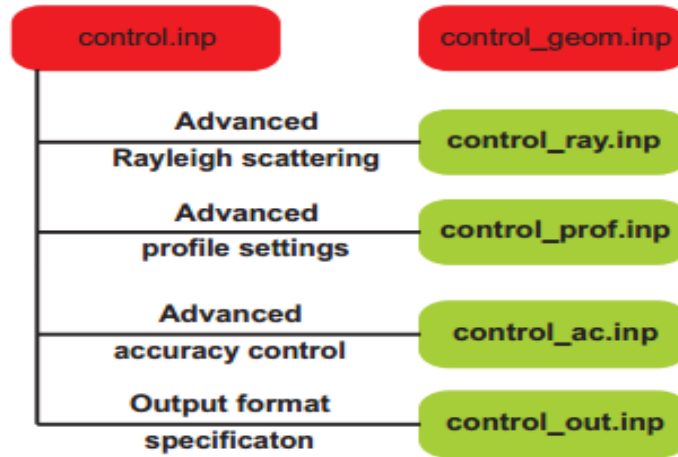
Figure 7: Main parameter files used in SCIATRAN to simulate polarisation (Rozanov et al., 2016)

SCIATRAN is a program to perform simulations of radiative transfer in the atmosphere and in the ocean, and includes a retrieval algorithm. Radiance spectra in the UV, visible and TIR spectral range are examples of the possible simulations. SCIATRAN can be used to model the radiance in the ocean-atmosphere system. SCIATRAN was originally designed to simulate radiances measured from the GOME and SCIAMACHY satellite spectrometers (Rozanov et al., 2016), but can also be

applied to other geometries.

Other capabilities of SCIATRAN include the ability to model intensities, to model Stokes vectors for the different polarisation and scattering cases (single or multiple), to describe weighting functions for scalar and vector cases, as well as to assess variables related to DOAS, such as, among others, air mass factors (AMF), which describe the effective light path in the entire atmosphere, slant columns, vertically resolved AMFs (box AMFs), and vertical optical depths (Rozanov et al., 2014).

Additionally, for the geometry considerations, the radiative transfer model can be run for different observation geometries and places of the instrument, either on the ground, in the atmosphere, at the water surface or in space. The main control files to run the simulations with SCIATRAN in this study are illustrated in Figure 7.

5 Methods

5.1 Differential Optical Absorption Spectroscopy (DOAS)

DOAS is a technique used to determine trace gas amounts using the absorption bands in the ultraviolet (UV), visible (vis), and near infrared (NIR) spectral range. This technique has been used to retrieve information on atmospheric trace gases, and is used to study the different gas distributions in the atmosphere. When natural light sources are being used, such as the Sun or the Moon for the DOAS method, it is called passive DOAS. The method is based on the separation of the high and the low frequencies in the absorption bands. The higher frequencies are being used to measure molecular absorptions, while the lower frequencies are being used to study scattering processes such as Rayleigh and Mie scattering (Platt and Stutz, 2008). The DOAS technique is based on Lambert-Beer's law, which describes the absortion process in general. The change of intensity $I(\lambda)$ in a thin layer of length L, concentration ρ, and absorption cross-section $\sigma(\lambda)$ is given by:

$$I(\lambda) = I_0(\lambda)exp(-\sigma(\lambda)\rho L) \tag{14}$$

where $I_0(\lambda)$ is the initial intensity, and $I(\lambda)$ is the intensity after interaction with the layer. Solving for ρ, the concentration can be given by:

$$\rho = \frac{ln(\frac{I_0(\lambda)}{I(\lambda)})}{\sigma(\lambda)L} = \frac{D}{\sigma(\lambda)L} \tag{15}$$

where D is the optical density of a layer of the given absorber. However, equation (14) needs to be modified, since it only works for the general case. In reality, there are several factors that affect the absorption of intensity of trace gases, as well as influence external factors such as the light path. For instance, absorption by several traces gases with concentrations ρ_j, absorption cross-sections $\sigma_j(\lambda)$ as well
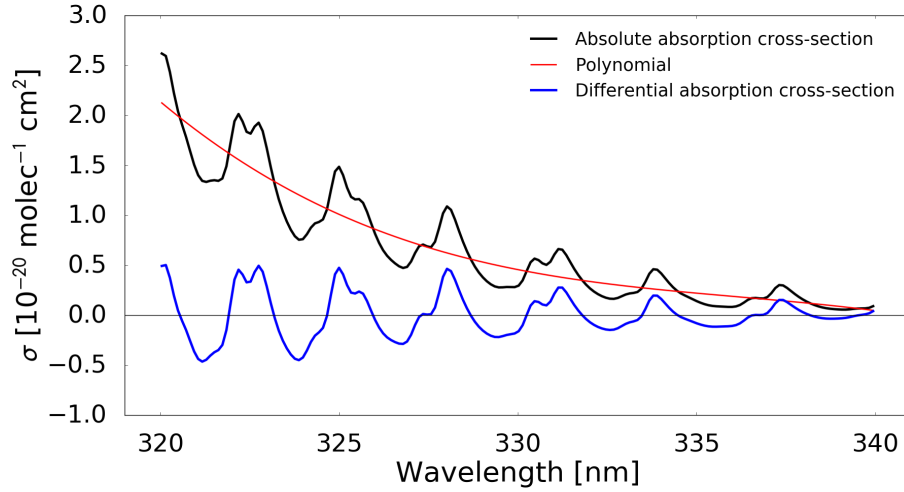
Figure 8: Principle of differential absorption cross-section

as, Rayleigh $\epsilon_r(\lambda) = \sigma_{Ro}\lambda^{-4}\rho_{air}$ and Mie extinction $\epsilon_M = \sigma_{Mo}(\lambda)\lambda^{-n}N_A$ need to be considered, which can be accounted for by:

$$I(\lambda) = I_0(\lambda)exp[-L(\sum(\sigma_j(\lambda)\rho_j) + \epsilon_r(\lambda) + \epsilon_m(\lambda))] \qquad (16)$$

By separation of absorption into the high and low frequencies, the absorption cross-section $\sigma_j(\lambda)$ can be rearranged into two cross-sections (see Figure 8):

$$\sigma_j(\lambda) = \sigma_{j0}(\lambda) + \sigma_j'(\lambda) \qquad (17)$$

where the first term tends to vary slowly with wavelength λ, which is part of the molecular absorption, and the second term corresponds to rapid variations with λ. For very small changes in the cross section along to the path of light, the integrate of the absorber column, known as the slant column density $SC = \int \rho(l)dl$, needs to be considered. Thus, taking into account the previous approximation for Rayleigh and Mie scattering, the final intensity after the absorption process can be written as:

$$I(\lambda) = I_0(\lambda)exp[-(\sum(\sigma_j'(\lambda)SC_j) - \sum(b_p\lambda^p))] \qquad (18)$$

where the first term of the summation corresponds to the narrow band absorption, and the second one is a polynomial approximation for the broad band signals.

5.2 The Air Mass Factor

DOAS uses two variables which allow the interpretating of scattered light observations, namely, the vertical column (VC) and the slant column (SC). The first one describes the amount of absorber integrated along the vertical column, and the second one represents the concentration integrated along the light path. Both are linked by the air mass factor (AMF), which is given by:

$$AMF = SC/VC \qquad (19)$$

For an unknown trace gas profile and altitude interval, the AMF can be expressed by the block-AMF or Box-AMF (Borrell et al., 2012) which is defined as:

$$BAMF_i = \frac{\partial SCD_i}{\partial VCD_i} \qquad (20)$$

The $BAMF_i$ is used to characterize the altitude-dependent sensitivity. The subscript is employed to describe the partial AMF for a given atmospheric layer. The terms SCD_i and VCD_i represent the partial slant and the vertical columns for certain layers of the atmosphere.

5.3 Multi-Axis DOAS (MAX-DOAS)

MAX-DOAS means multi-axis DOAS, and denotes scattered light observations taken under several elevation angles. Using this method, the sensitivity to the lower troposphere is enhanced as for this region, the light path is elongated at low viewing elevations (Platt and Stutz, 2008). Additionally, vertical profiles can be estimated using measurements under several viewing directions. A sketch of typical light paths for multi-axis DOAS applications is given in Figure 9. Light coming from the Sun crosses the atmosphere and is scattered at low viewing geometries towards the ground based instrument.
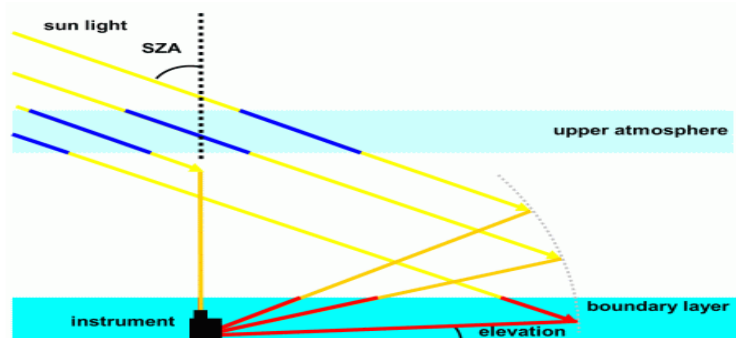
Figure 9: Multi-Axis DOAS (MAX-DOAS)
`http://www.iup.uni-bremen.de/doas/maxdoas_instru\%ment.htm`

5.4 DOAS and polarisation

By using a DOAS instrument equipped with a polarizer, it is possible to make a series of measurements of polarisation in the atmosphere at different directions, which in turn can be used to validate SCIATRAN calculations.

From measurements of sky-light intensities by the DOAS instrument, polarisation can be detected in perpendicular direction with respect to the plane of scattering (90°). However, during the scattering process, Raman and Rayleigh scattering take place in parallel and perpendicular direction, respectively. Thus, a measure of the intensities in those directions allows the study of the so called Ring effect (Platt and Stutz, 2008).

The Ring effect shows a change in the depth of the solar Fraunhofer lines perceived in scattered light, which is slightly less intense than those observed for direct sunlight (Vountas et al., 1998). This effect is related to the change of wavelength from the incoming light due to Raman scattering, which also has a subtle effect on the polarisation of scattered light. Unpolarized Raman scattered photons cause a filling in process of the Fraunhofer lines. Hence, polarisation features in Fraunhofer lines are present in the scattered light spectrum (Aben et al., 1999).

Furthermore, by measuring polarisation from different directions in the atmosphere, information about the type of aerosols or cloud parameters can be obtained. For instance, by estimating the degree of depolarisation, properties of the sphericity of atmospheric components can be derived (Wagner et al., 2004).

The measurement instrument itself can be polarisation dependent, which leads to problems in DOAS measurements if no measures are taken to make the instrument unpolarised, for example by using a long quartz fibre, or by measuring polarisation and by correcting for the effect as done for the Global Ozone Monitoring Experiment (GOME) instrument (Burrows et al., 1999).

5.5 The DOAS setup

A DOAS instrument consists of a grating spectrometer, a Charged Coupled Device (CCD) detector, a telescope to point at different elevation angles, a quartz fiber bundle connecting the spectrometer and the telescope, a computer to register the measurements, and a control system which monitors the measurements. The incoming light from the atmosphere comes into the telescope, and its signal is registered by the spectrometer through the quartz fiber bundle.

To take care of polarisation measurements in the different components of the instrument, it is required to know to which extent the spectrometer is sensitive to the different polarisation states of sky-light (Carlson et al., 2010). Optical components
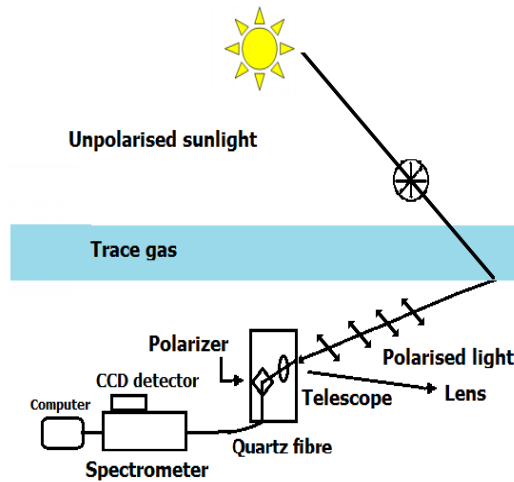
Figure 10: DOAS Setup

such as mirrors or gratings polarize the reflected light. More importantly, the efficiency of a reflective grating depends on the polarisation state of the light, which can lead to problems when used for atmospheric measurements. By the use of the quartz fibre bundle, the polarisation state of incoming light is scrambled, strongly reducing the degree of polarisation at the entrance of the spectrometer, which is important for good DOAS measurements. Thus, to measure polarisation from incoming light of the atmosphere, the polarizer should be set in front of the quartz fibre.

5.6 The thesis experiment

For the experiments performed in this thesis, the DOAS instrument from IUP was equipped with a Glan-Thompson polarizer set into a motorized turntable. The polarizer was mounted in front of quartz fibre bundle in the telescope.

After that, a long cable was created to control the polarizer from a computer operated in the building. Then, with the assistence of André Seyler, a PhD student in the DOAS group, a data cable was efficiently created and tested along with the polarizer and the DOAS instrument. After that, measurements of intensity (radiance) in the atmosphere were performed at different polarisation angles, as will described below.

The measurements were taken in Bremen in the period of 24 September to 31 October of 2017. The instrument was pointed at different lines of sight and relative different azimuth angles, and was operated throughout the day. In this way, the Bremen MAX-DOAS instrument, which covers the wavelength ranges 305-390 nm and 409-580 nm, could measure as well the UV as the visible range.
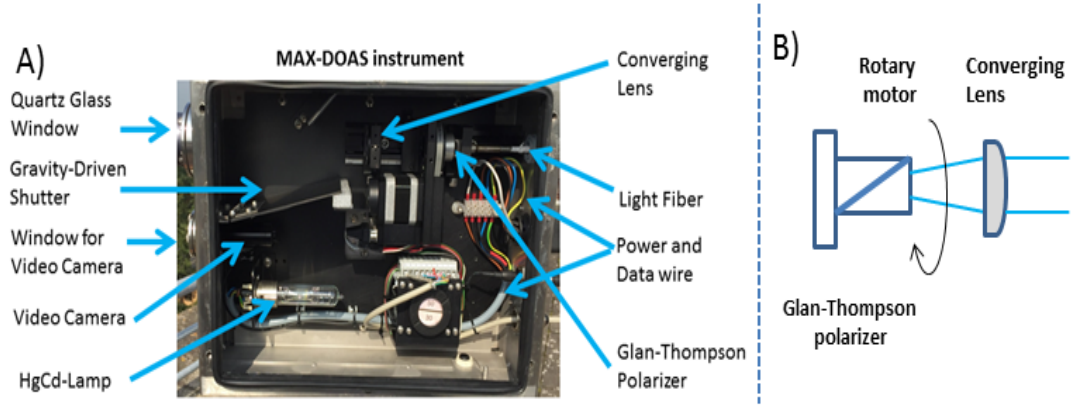
Figure 11: MAX-DOAS Instrument. A) Components of Bremen MAX-DOAS instrument. B) Function of the polarizer for the measurements

The measurements were divided in the following steps:

i) First, one Almucantar scan (20° azimuthal steps) was performed, followed by one Principal plane scan (10° elevation steps), roughly every 90 minutes. Each measurement was repeated 4 times with the following polarizer positions relative to the viewing direction: -45°, +45°, 0°, 90°.

ii) In between the different scans, normal DOAS measurements were performed, wherein always one measurement was taken in parallel position and one in perpendicular position (0°, 90°) of the polarizer. Computation of I, Q, U and the degree of polarisation DLP followed the method described by (Kreuter et al., 2010).

iii) Finally, from the equations presented below (Equation 21 and 22), the Stokes parameters I, Q, U, and the degree of polarisation DLP were computed. The results and description of the plots will be given in Chapter 6.

$$\begin{bmatrix} I \\ Q \\ U \end{bmatrix} = \begin{bmatrix} R_0 + R_{90} \\ R_0 - R_{90} \\ R_{45} + R_{45} \end{bmatrix} \tag{21}$$

The degree of linear polarisation (DLP) given by:

$$DLP = \frac{\sqrt{Q^2 + U^2}}{I} \tag{22}$$

6   Results

6.1   SCIATRAN simulations

The simulations of polarisation were done using SCIATRAN version 3.7.1 under the scenarios described in Table 1.

Table 1: SCIATRAN simulations data settings. Line of sight (LOS)[°] in steps of 1° from 90° to 100° and steps of 2° from 100° to 180°, SZA[°] in steps of 10° up to 80°, RAA[°] in steps of 5° from 0° up to 180°, and steps of 10° from 180° to 360°
* continental, maritime and urban aerosols

SCIATRAN POLARISATION SIMULATIONS		
	1st scenario	2nd scenario
	Rayleigh atmosphere	Aerosol* atmosphere
Multiple scattering	✓	✓
pseudo-spherical geometry	✓	✓
Albedo (A)	$A = 0$	$A = 0$
LOS[°]	90 to 180	90 to 180
SZA[°]	0 to 85	0 to 85
RAA[°]	0 to 360	0 to 360
λ[nm] in steps of 50	350 to 550	350 to 550

6.2   SCIATRAN simulation for Rayleigh atmosphere

The simulation of polarisation in pseudo-spherical geometry was performed using SCIATRAN version 3.7.1 for a Rayleigh atmosphere, with multiple scattering and with albedo equaled zero. The line of sight (LOS) was set to range between 90° and 180° degrees, the solar zenith angle (SZA) to range between 30° and 85° degrees in steps of 10°, and the azimuth angle to range from 0° up to 360° degrees. Figure 12 (first row) shows the Stokes components (I, Q, V) from data simulation and the degree of linear polarisation (DLP), at the surface for a wavelength of 350nm. This first row of Figure 12 displays the almucantar plane projection, which is generated by an azimuthal scan, and it is represented as a concentric circle around the zenith, as is shown therein.

The low intensity values are concentrated perpendicular to the Sun direction, in agreement with the phase function of Rayleigh scattering (see Figure 4), since at 90°, the phase function has low values, and for the forward and backward direction it has a maximum. The degree of linear polarisation DLP is given by equation (22).

DLP shows high values at directions perpendicular to the Sun as is shown with the reddish dark color in the plot of DLP (Figure 12). This is because Rayleigh scattering under 90° scattering angle is strongly polarizing. In the second row, all variables are plotted against the (LOS) for different SZA. The behavior of p for the line at 60° SZA is almost equal to that for 30° SZA, so that the maximum of DLP

tends to be similar for these two SZA, showing that the degree of polarisation for its maximum is independent of the SZA.
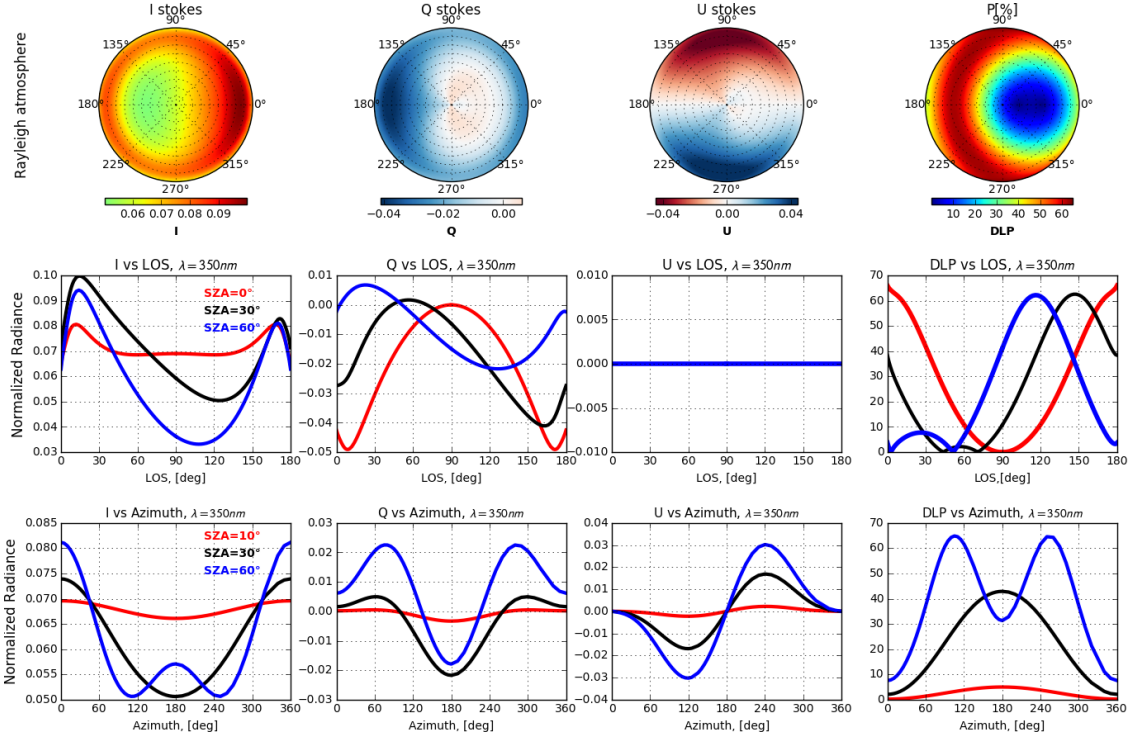

Figure 12: Radiance simulation for multiple scattering at 350nm, different LOS (diff LOS) and different azimuth (diff Azim) , SZA equals $30°$ and solar azimuth angle equals $0°$. The radiance values are normalized to the extraterrestrial irradiance. First row shows the Stokes components and the *DLP*, in short *p*. Second row displays the Stokes components in the solar principal plane at different SZA; the third row represents the Stokes components in the solar almucantar plane also for different SZA.

The second row in Figure 12 shows the Stokes components in the solar plane. Most of them are relatively similar at different SZA. In the case of the *I* Stokes component, it has a higher radiance at $30°$ SZA compared to $60°$ SZA and $0°$ SZA, as opposed to the *Q* Stokes component, because at $60°$ SZA, *Q* is higher than the *Q* at $30°$ SZA and at $0°$ SZA. In the latter situation, *Q* shows more negative values. The *U* Stokes component is zero for all SZA due to symmetric arguments in the definition of *U* ($U = <E_l E_r^* + E_r E_l^*>$, $E_l E_r$, parallel and perpendicular electric fields, * defines complex conjugate).

Finally, the third row shows the variation of the Stokes components with respect to the azimuth in the almucantar plane projection. The plot was generated for constant SZA values of $10°$, $30°$ and $60°$. For this case, the *DLP* at $60°$ reached the

same maximum value as in the second row for the principal plane projection. The other values of *DLP* in the almucantar plane were lower than the values present in the row 2 of Figure 12. Therefore, when the SZA angle increases for the almucantar view, the *DLP* also becomes higher.
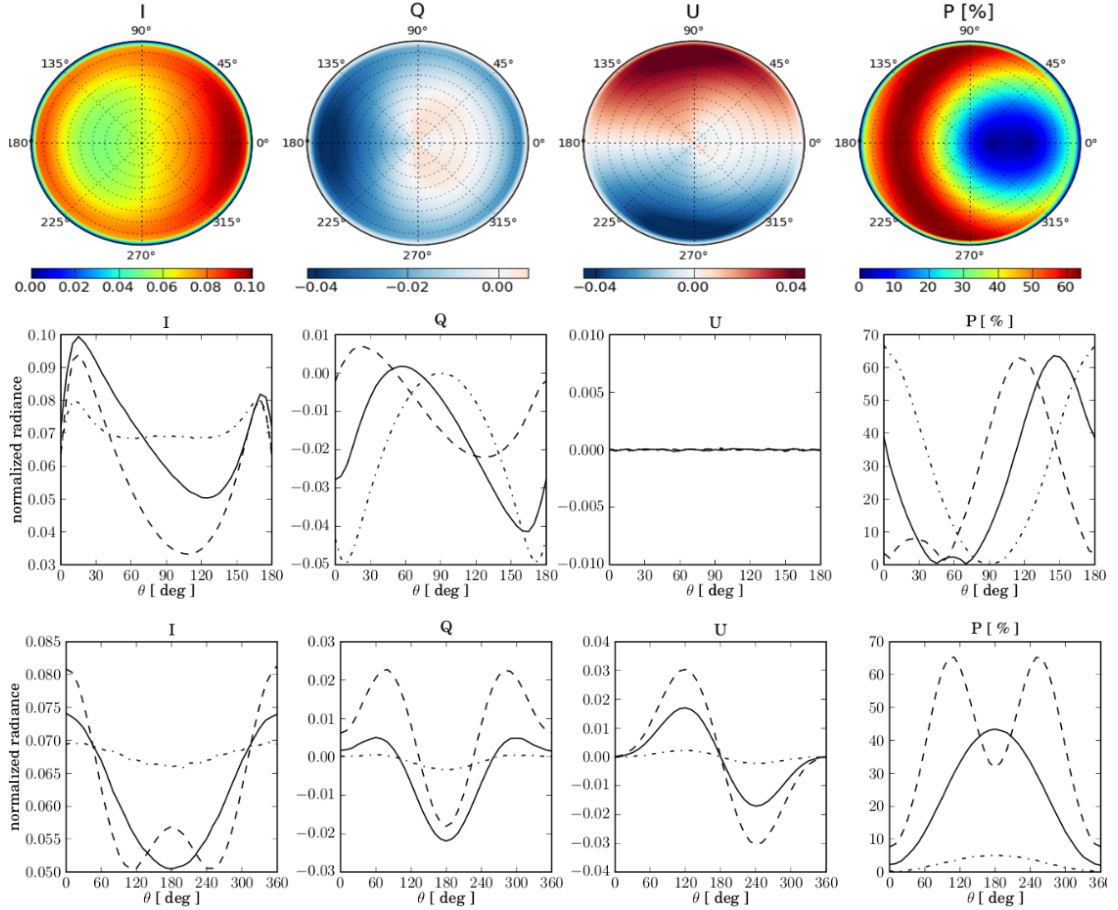

Figure 13: First row: simulated Stokes components and degree of polarisation (p) for downwelling radiation at 350 nm for a solar zenith angle of 30° in a Rayleigh atmosphere. Second row: Stokes components *I, Q, U* and p in the principal plane projection. Third row: Stokes components *I, Q, U* and p in the almucantar plane projection (published by (Emde et al., 2010).

6.3 Comparison of SCIATRAN polarisation simulations for a Rayleigh atmosphere to Emde et al.,(2010)

The same simulations as performed with SCIATRAN which are shown in Figure 12, have been performed by Emde et al., 2010 and are shown in Figure 13. The conditions for the SCIATRAN calculations in this thesis were selected to match those from this publication in order to allow direct comparison. As can be seen, there is an excellent agreement for all simulation conditions, SZA, geometries, LOS,

and for the azimuth angles for all the Stokes components (see Figures 12 and 13). This is taken as verification for the choice of simulation parameters and used as a starting point for further simulation experiments.

6.4 Wavelength dependency of the SCIATRAN polarisation simulation for a Rayleigh atmosphere

The Stokes parameters I, Q, U and the DLP, and how they change over different wavelengths, are shown in Figure 14. The odd rows display their variation in the principal plane projection for SZA values of $0°, 30°, 60°$ (red, blue and black lines). Also, it shows the variation of the Stokes components when the wavelength is increasing from 350nm up to 550nm. The even rows represent the almucantar plane projection where the SZA was set to $0°, 30°$, and $60°$.

In the two different types of plane projections (almucantar and principal), a decrease was found in the magnitude of the Stokes parameters, as indicated by the shape of their curves. In the principal plane, the I component changed slightly for all SZA, with the lowest normalized radiance values ranging between $30°$ and $150°$ LOS. The maximum values remained close to $0°$ and $180°$ LOS. The Q parameter for the three SZA changed in a different way at $30°$ and at $60°$, but for $0°$ it was almost the same as seen for all the other wavelengths. Also here, just as with I, Q remained constant between $30°$ and $150°$ LOS, with a normalized radiance which equaled zero. The U Stokes components were the same for all SZA, and the wavelength range, with a constant normalized radiance, which remained equal to zero due to symmetry reason, as was described in Section 6.2.

For the almucantar plane projection, all the Stokes parameters follow the same pattern when the wavelength is increased, but they decrease slightly and become almost zero by a normalized radiance. For only few magnitude units, the values of I and Q are bigger than in the principal plane projection. The behavior of U in the almucantar plane is quite different from the U in the principal plane. However, independent of the plane projections, the DPL is increasing when the wavelength increases as well.

In contrast to the reduction in magnitude of the Stokes components, the DLP is high. In the principal plane, it increased in a similar way for all SZA. Nevertheless, for the almucantar plane, the increment of DLP was totally different for every SZA. At $60°$ SZA, the degree of linear polarisation becomes higher every time when the wavelength was increased. However, at $10°$ and at $30°$, the DPL rises very slowly. For both planes projection at $60°$ SZA, the DLP was the same value in all increments of wavelength. For the other SZA, the DLP was higher in the principal plane than in the almucantar plane. At the largest wavelength, the DLP was higher with a value of approximately 90%.

The increment of DLP when λ increases is related to the scattering of light. The scattering of light is stronger at shorter wavelengths, and therefore multiple scattering is more important. As multiple scattering decreases polarisation, the DLP is smaller at UV wavelengths than at the visible part of the spectrum.

## 6.5   SCIATRAN polarisation simulation with aerosols

A second simulation was performed using the same conditions as described in Section 6.1 and Table 2. However, for this simulation continental, urban and maritime aerosols were included. All of them used the same Aerosol Optical Depth (AOD) and vertical profile. Figure 15 displays the results obtained in polar projection (first row). The second row shows a simulation for water aerosol data from (Emde et al., 2010), all of them for a wavelength of 350nm.

Table 2: SCIATRAN polarisation simulation using aerosols at an Aerosol Optical Depth (AOD) equal to 0.1 and with a vertical profile. Aerosol*: Continental, Maritime and Urban
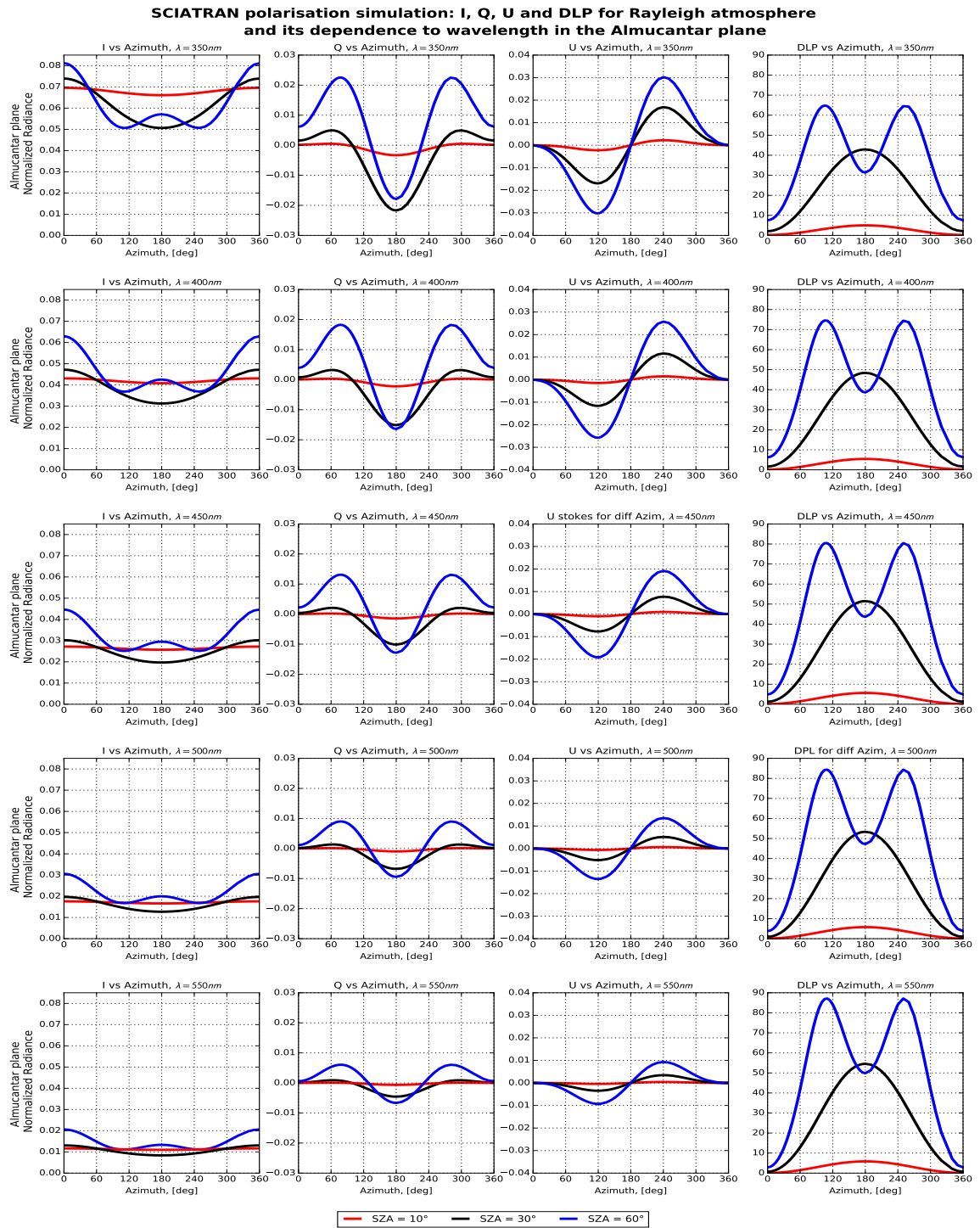
SCIATRAN polarisation for aerosols	
height (km)	Aerosol* AOD
0	0.1
2	0.1
3	2.50×10^{-4}
12	2.50×10^{-4}
13	2.50×10^{-4}
20	2.18×10^{-4}
30	3.32×10^{-5}
35	2.45×10^{-5}
40	8.00×10^{-6}
45	4.02×10^{-6}
50	2.10×10^{-6}
70	1.60×10^{-7}
100	9.3×10^{-10}

By a simulation employing aerosols in SCIATRAN, the Stokes components were very similar to Emde's publication. However, the main observed differences in both cases are expected to be related to the type of aerosols. Additionally, the observed reduction in the values for the Stokes parameters as well as the DLP were considerable in respect to the simulation without aerosols (see Figure 13).

Furthermore, for aerosol simulations performed by SCIATRAN, the observed intensity in respect to the values observed by (Emde et al., 2010) was a few units
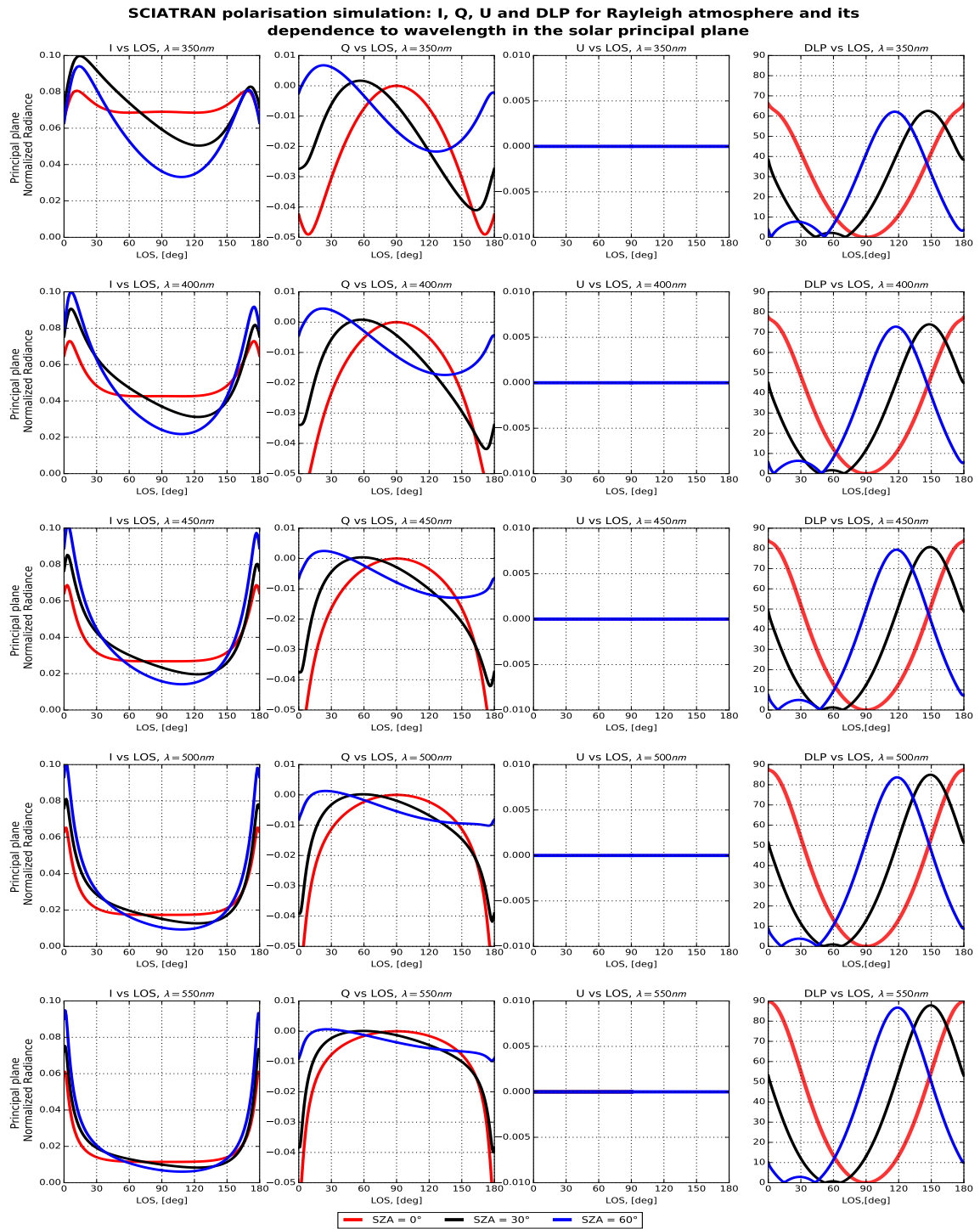
Figure 14: Wavelength dependency for SCIATRAN polarisation results, using a Rayleigh atmosphere and SZA at $0°, 30°, 60°$ for principal plane projection.

Figure 15: Wavelength dependency for SCIATRAN polarisation results, using a Rayleigh atmosphere and SZA equals $10°, 30°, 60°$ for the almucantar plane projection.
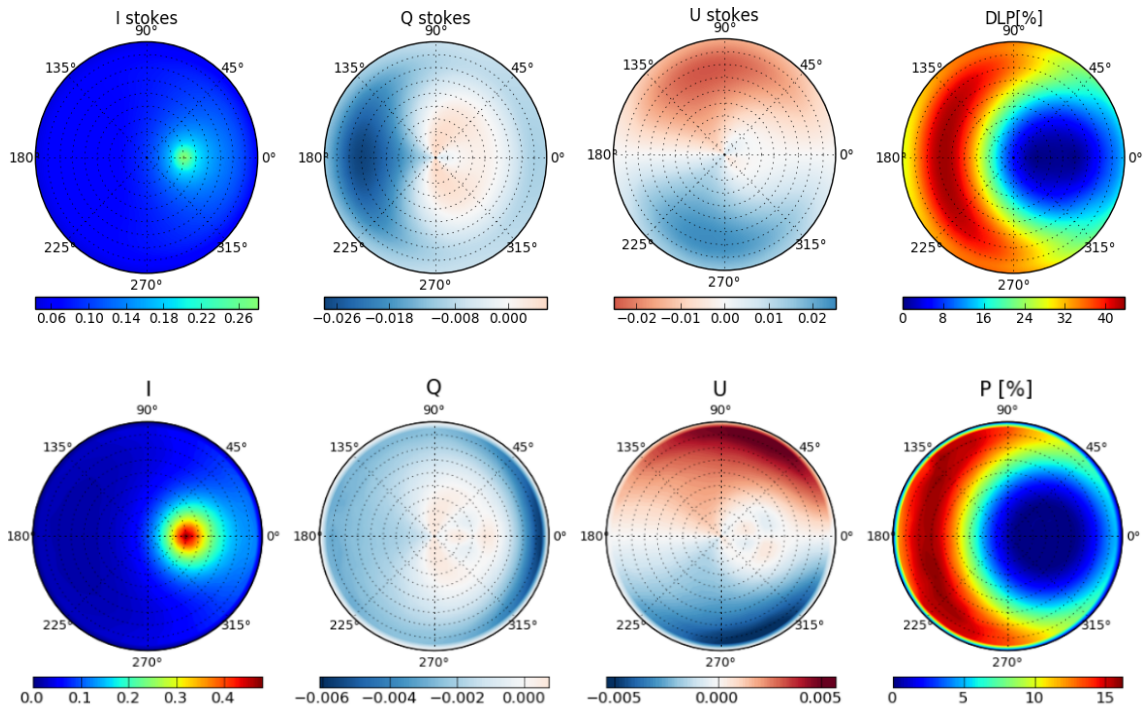
Figure 16: Simulated Stokes components and degree of polarisation for down-welling radiation at 350 nm for a solar zenith angle of 30°. The simulation for water soluble is for an atmosphere consisting only of aerosols (Emde et al., 2010).

lower for the continental and urban aerosols. Nevertheless, maritime aerosol displayed higher intensities than the computed values by (Emde et al., 2010).

Additionally to the intensity results, the *DLP* by SCIATRAN simulation reached 50% and was the same value for all the three types of aerosols employed.
Only for scenario B (second row in Figure 16), a similarity in the shape and magnitude of *DLP* was found between the study of (Emde et al., 2010) and the SCIATRAN simulations. Nevertheless, the main differences can be explained by the use of different AOD's and the setting conditions for aerosols in both cases.
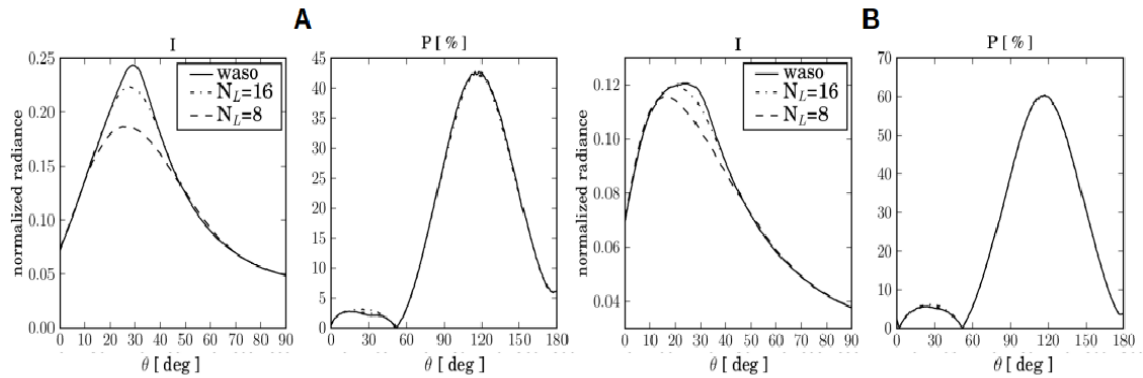
Figure 17: A) Intensity and degree of polarisation in the solar principal plane for an aerosol optical thickness of 0.5. Assuming that all aerosols corresponds to one aerosols type as defined in Optical Properties of Aerosols and Clouds (OPAC) . B) Intensity and degree of polarisation in the solar principal plane for an aerosol optical thickness of 0.5 and 0.05 (Emde et al., 2010).

6.6 Comparison of SCIATRAN polarisation simulations for an atmosphere with aerosols to Emde et al.,(2010)

Figure 16 shows the aerosol simulation for water soluble (waso) and salt accumulated mode (ssam) using the MYSTIC model and Delta M, with scaled optical properties with 8 and 16 Legendre terms (Emde et al., 2010) displayed with dotted and dashed lines in the second row of Figure 16. In a similar way, and by aiming to reproduce the plots as shown in Figure 17, the simulation for an atmosphere with aerosols using SCIATRAN was done for continental, urban and maritime aerosols. All of them are slightly different than the OPAC aerosols.

The best agreement with simulations from (Emde et al., 2010) was found for the simulation performed for the continental aerosols, as can be seen in Figure 17. Comparing the results for different aerosol types, the main difference is the magnitude of the forward scattering peak at LOS =30°. This is determined by the size parameter (see Figure 6) and is much stronger for the larger maritime aerosols. The *DLP* was almost the same in all cases, with very small differences, and reached a maximum value around 50%, as is shown in Figure 16.
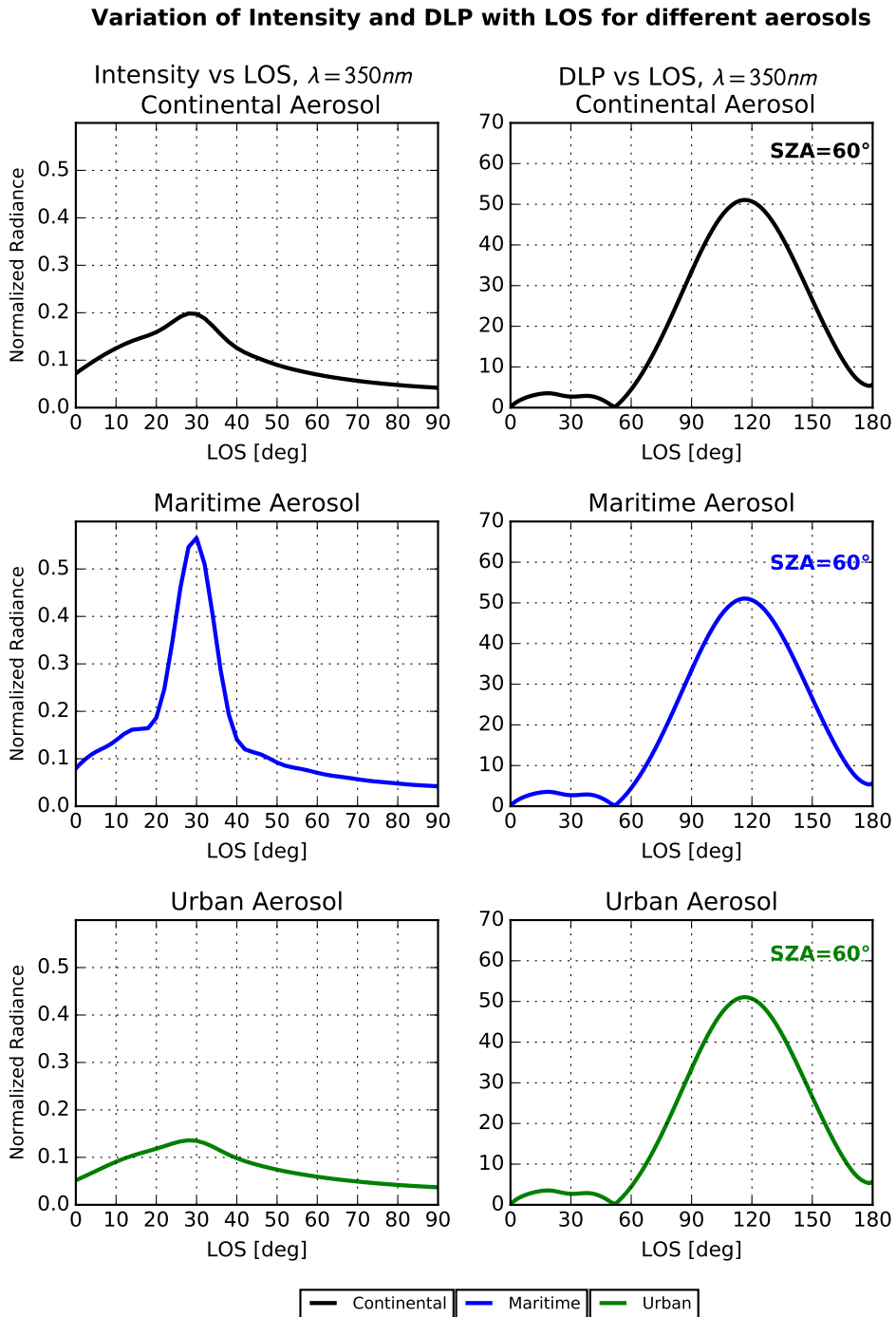
Figure 18: Intensity (I Stokes component) and $DLP[\%]$ in the principal solar plane using SCIATRAN simulation for different types of aerosols and for a reference wavelength of 337nm for the extinction coefficient profile. Aerosol optical thickness of 0.1. The graphics were created for SZA = 60° for all scenarios and plotted for a wavelength of 350nm. The first row is for continental aerosol, the second one is for maritime aerosol, and the last one corresponds to urban aerosols.

6.7 SCIATRAN polarisation simulations for an atmosphere with continental aerosols and for all wavelengths

In order to see how the DLP changes with respect to the wavelength, the continental aerosols were selected because they offer the best agreement to the plot B in Figure 16. After that, the intensity and DLP were computed for a range of wavelengths from 350nm in steps of 50nm up to 550nm, as is shown in Figure 18. The DPL increases with larger wavelengths, and has a maximum value of 60% at 550nm, and a minimum value above of 50% at 350nm. This is the result of a decreasing contribution of multiple scattering at larger wavelengths, because of the decreasing Rayleigh scattering cross-section.
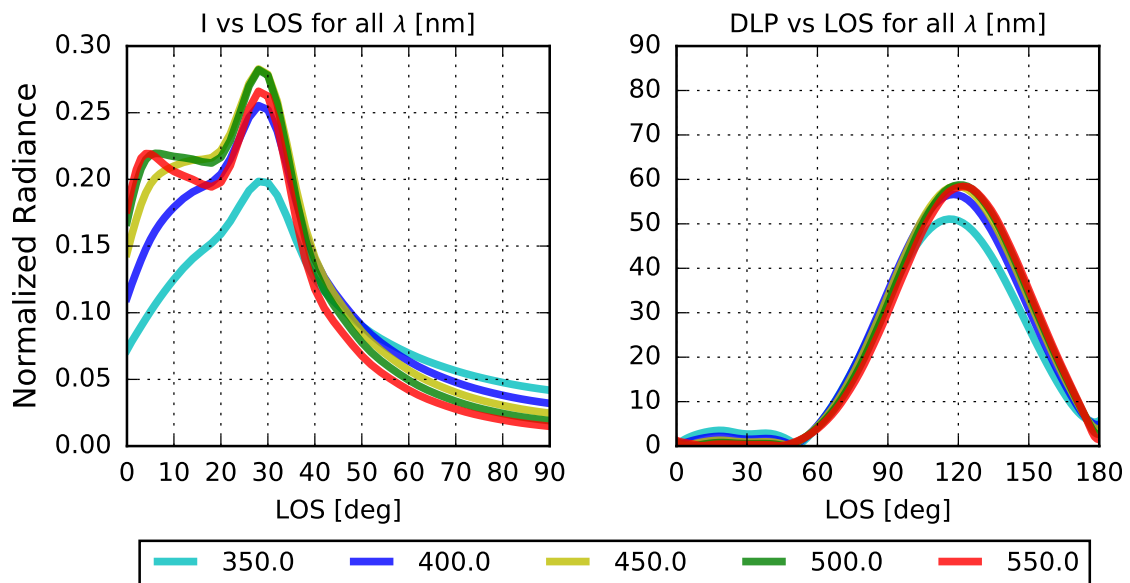
Figure 19: Intensity (I Stokes component) and $DLP[\%]$ in the principal solar plane using SCI-ATRAN simulation for continental aerosol and a reference wavelength of 337nm for the extinction coefficient profile. Aerosol optical thickness of 0.1. The graphics were created for SZA = 60° for all wavelength range from 350nm in steps of 50nm up to 550nm.

6.8 SCIATRAN polarisation simulations for an atmosphere with urban aerosols: effect of varying the AOD

By the use of SCIATRAN polarisation simulations, a new running was performed for the case of urban aerosols with different values of AOD and different vertical profiles, with the settings as shown in Table 3.

Table 3: SCIATRAN simulation: urban aerosol at different AOD and vertical profile. AOD* settings for urban aerosol.

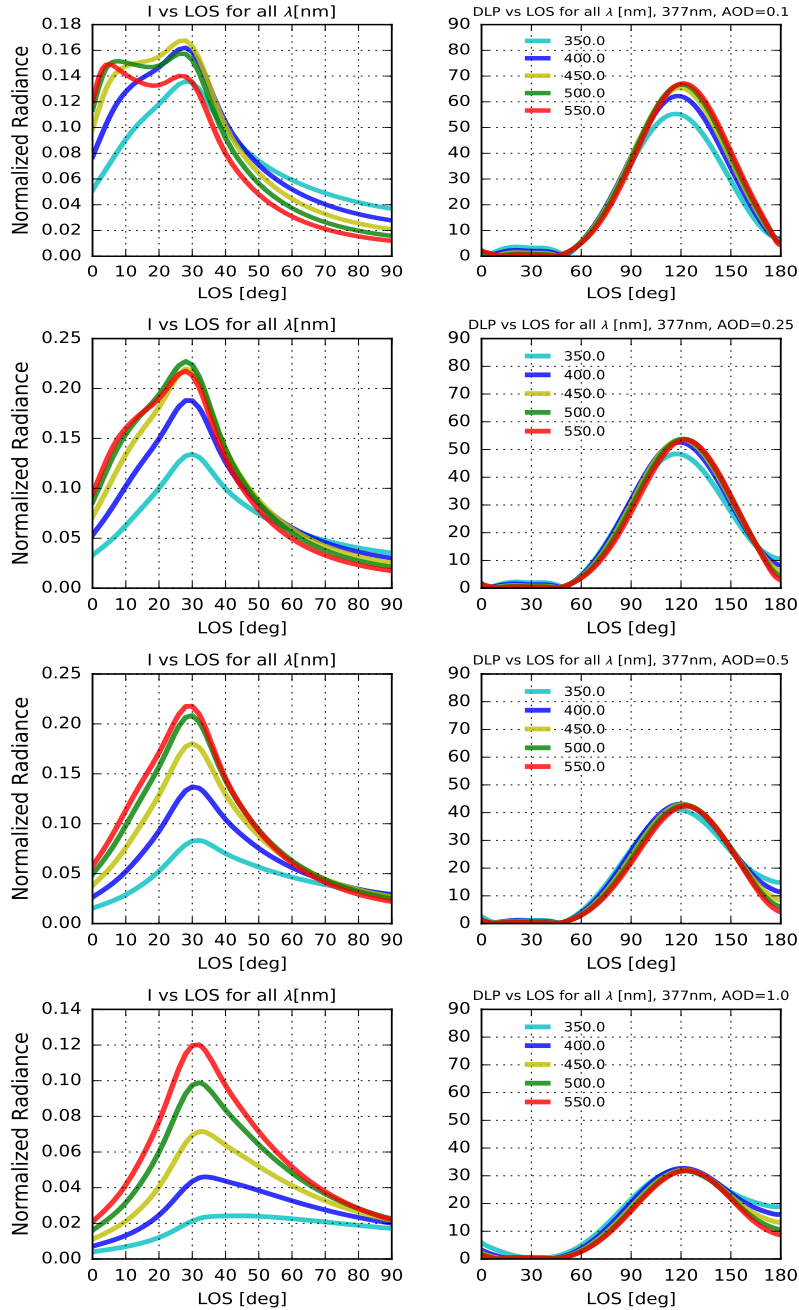| SCIATRAN simulation for urban aerosol				
height (km)	AOD1*	AOD2*	AOD3*	AOD4*
0	0.1	0.25	0.5	1
2	0.1	0.25	0.5	1
3	2.50×10^{-4}	6.25×10^{-4}	1.25×10^{-3}	2.50×10^{-3}
12	2.50×10^{-4}	6.25×10^{-4}	1.25×10^{-3}	2.50×10^{-3}
13	2.50×10^{-4}	6.25×10^{-4}	1.25×10^{-3}	2.50×10^{-3}
20	2.18×10^{-4}	5.45×10^{-4}	1.09×10^{-3}	2.18×10^{-3}
30	3.32×10^{-5}	8.30×10^{-5}	1.66×10^{-4}	3.32×10^{-4}
35	2.45×10^{-5}	6.13×10^{-5}	1.23×10^{-4}	2.45×10^{-4}
40	8.00×10^{-6}	2.0×10^{-5}	4.00×10^{-5}	8.00×10^{-5}
45	4.02×10^{-6}	1.01×10^{-5}	2.01×10^{-5}	4.02×10^{-5}
50	2.10×10^{-6}	5.25×10^{-5}	1.05×10^{-5}	2.10×10^{-5}
70	1.60×10^{-7}	4.00×10^{-7}	8.00×10^{-7}	1.60×10^{-6}
100	9.3×10^{-10}	2.325×10^{-9}	4.65×10^{-9}	9.3×10^{-9}

When the AOD was increasing, the dependency of the I Stokes parameter and the DLP for different AOD's displayed a decrement in the DLP. However, the Stokes parameter I had a different behavior. For AOD values of 0.25 and 0.5, I was higher than the case of the other AOD situations. The highest DLP is given by an AOD of 0.1, while the lowest is found for an AOD which equals 1.0, as is shown in Figure 20, employing the same wavelength range as in Figure 19.

In general, the variation of DLP in respect to the wavelength range was a few units different for all used sets of AOD's. Only at 0.1 AOD, small differences were observed. Nevertheless, for the other AOD, the maximum value of DLP was the same for each scenario, as is shown again in Figure 20.

As the DLP changes due to the increase in AOD, an AOD of 0.5 was used with the aim to reproduce similar results as shown in Figure 17A. The variation of I and DLP can also be explained in terms of the chosen wavelengths (377, 400, 488, 515 and 550nm) for the aerosol extinction profile. Thus, the findings show acceptable values in respect to Figure 17A from (Emde et al., 2010), since similar values of

intensity and *DLP* were found, as shown in the first row of Figure 21. For the other rows in the same figure, the *DLP* decreases slightly when the wavelength for the extinction profile increases, while, at the same time the *I* values are reduced in small proportions.

Figure 20: SCIATRAN polarisation simulation for urban aerosols at different AOD and wavelength of 377nm for the coefficient extinction.
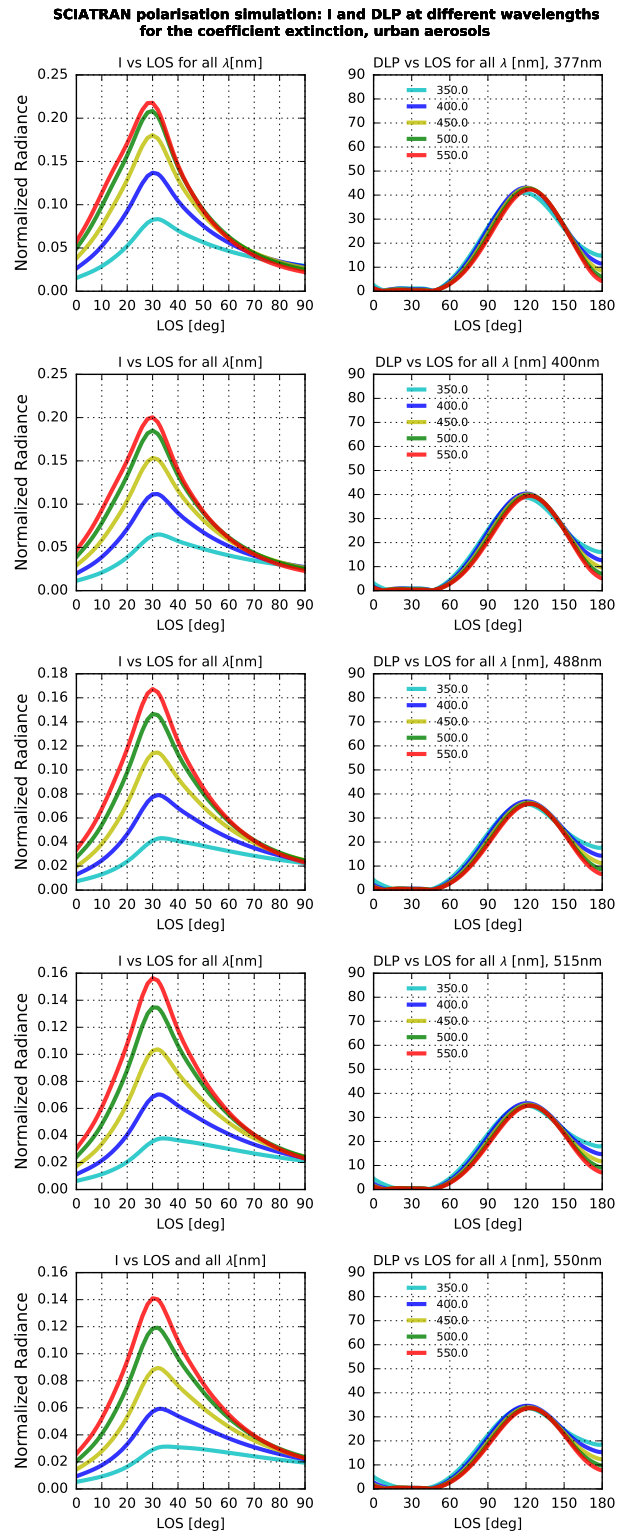
Figure 21: SCIATRAN polarisation simulation: intensity and *DLP* for urban aerosol with AOD equal to 0.5 and different wavelength for the coefficient extinction
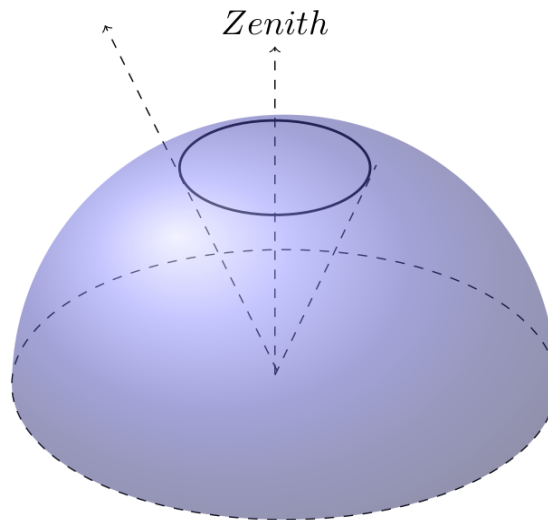
6.9 MAX-DOAS experiment: almucantar plane projection vs Relative Azimuth Angle in the UV

For the almucantar plane projection, the measurements were performed by pointing the telescope in the elevation angle of the Sun and varing the azimuth angles from $0°$ to 360 degrees in steps of $20°$. The small changes in SZA during the measurements were accounted for in the telescope elevation. An example of the process to collect the data measurements for the almucantar plane is shown by Figure 22. The solid and dash red lines denote the points were the data was obtained.
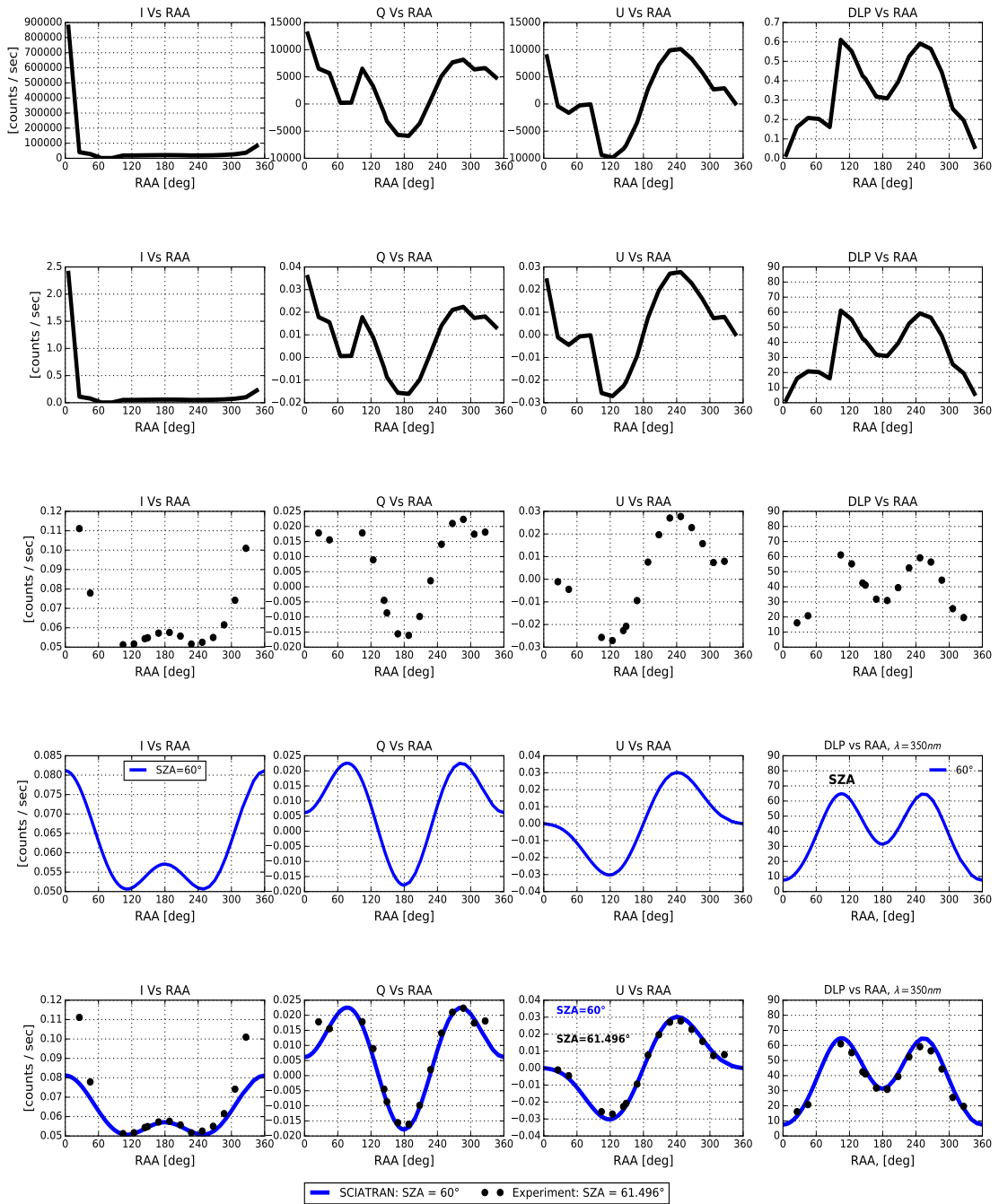

Figure 22: Almucantar plane projection geometry used for the MAX-DOAS measurements

The measurement for this case was performed on the 1st of October of 2017 over different time intervals. Figure 23 shows the case for the almucantar measurement from 9:07 to 9:26 with an experimental average value of SZA set equal to $61.496°$ and a relative azimuth angle (RAA) ranging between $0°$ to $360°$. The Stokes parameters I, Q, U, and DLP, or p in short way, were estimated from equations (21) and (22).

The resulting Stokes components are displayed in the first row of Figure 23. The collected data are given in arbitrary units for the y-axis for the I, Q, and U Stokes parameters. DLP is given in percentage units[%]. A problem during the measurements was that they were sometimes blocked by parts of the building, leading to data which could not be used. These points were identified by inspection of the images recorded by the video camera in the telescope, and were removed when detected. Also, data which was collected when pointing too close to the Sun was removed, because scattering of direct sunlight into the instrument affects either the measurements or the quality of the measurements. As the MAX-DOAS instrument is not radiometrically calibrated, the measurements provide radiance only in relative

Figure 23: Experimental data values of the day 01/10/2017 for the almucantar plane projection at 61.496° SZA and SCIATRAN simulation for SZA at 10°(red line), 30° (black line) and 60° (blue line) and 350nm wavelength.

units. In order to compare to SCIATRAN results, a scaling factor of $1/(3.65 \times 10^{-5})$ was applied which was determined by optimising the agreement for one case. This factor was then kept constant for all further comparisons.

Finally, the average of the SZA was once more estimated for the modified experimental data, and the observed variation relative to the original SZA was very small, as is shown in the fifth row of Figure 24. Thus, by the same process as with the other experimental data for the almucantar plane projection, we obtain Figure 24, where the dots represent measurements at different SZA and the lines are simulations for the SZA equal to 57°, 65°, and 76°. The use of a SZA for the simulation close or equal to the SZA given by the experiment, shows acceptable results in almost the whole RAA. Part of this good fit can be explained by the clear sky condition: no clouds were present at some time intervals during the collecting of the measurements. However, close to 0° and 360°, the observed unfit between the experimental measurements and the SCIATRAN simulations can be related to the fact that by SCIATRAN the Sun is always in the same position, while for the experimental measurement the position of the Sun was constantly moving.

6.10 SCIATRAN polarisation simulations and the MAX-DOAS experiment: Almucantar plane projection vs Relative Azimuth Angle for different SZA in the UV

As is shown in Figure 24, it is possible to observe the accuracy of the measurements and the simulation data for most of the SZA used in both situations as well as for every Stokes parameter and every DLP. However, for the simulation case of SZA equal to 76°, the fit in the I Stokes component was not so accurate for the experimental SZA when equal to 75.973°. The Q component was relatively accurate for all data, but not so many data for a SZA equal to 56.737° or 57° and between 0° to 60° or 300° to 360° in the relative azimuth angle were found. The simulate value is represented by the orange line in Figure 24. The U Stokes parameter shows the best agreement between the simulated and the experimental data. In respect to the DLP, there are two maximum values around 65% and it was almost the same for the simulated data as for the experimental data. Thus, the maximum value of DLP is independent of SZA, but for its minimum value the DLP tends to decrease for larger SZA.
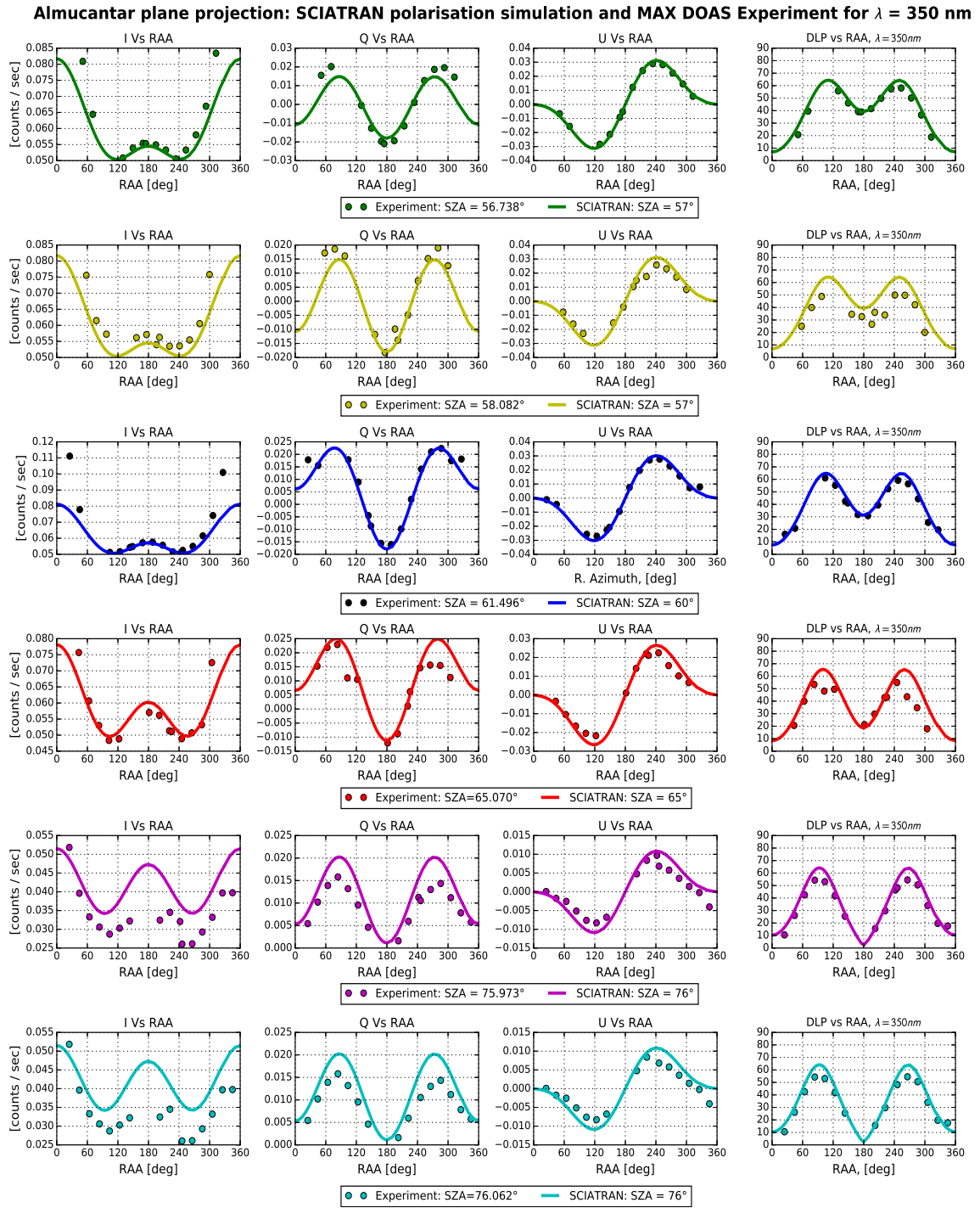
Figure 24: Experimental data values of the day 01/10/2017 for the almucantar plane projection at different SZA and SCIATRAN simulation for SZA at 57°(green and yellow lines), 60°(blue line), 65°(red line) and 76°(magenta and cyan lines) and a wavelength of 350nm.

6.11 Dependency on wavelength by the SCIATRAN polarisation simulations and the MAX-DOAS experiment in the almucantar plane projection

In addition to the graphics for the different SZA in the almucantar plane projection, a complementary study of the Stokes components and the DLP can be seen in Figure 25. In this figure, one can see that the dependency on the wavelength for SCIA-TRAN and for the MAX-DOAS measurements is very different. The SCIATRAN simulation is represented by the solid lines and the MAX-DOAS measurements are represented by dots (Figure 25). Both data are plotted for different SZA. The findings show an increment in the range of magnitude for the Stokes components estimated from the experimental measurements, while also for the measurements the DLP remained around 60% as a maximum for all the wavelengths used during the performance of the MAX-DOAS measurements.

In comparision with the SCIATRAN simulations, the Stokes parameters remained within the same range of magnitude given in the y-axis, and the main difference was observed in the DLP: it was increasing when λ increased as well. Although the profile of experimental I, Q, U and DLP was similar to the ones of the simulation, the estimations of the Stokes components from the experiment were higher than the values computed with SCIATRAN. Thus, even while there is an unfit between the measurements and the simulations, the DLP gives acceptable results.
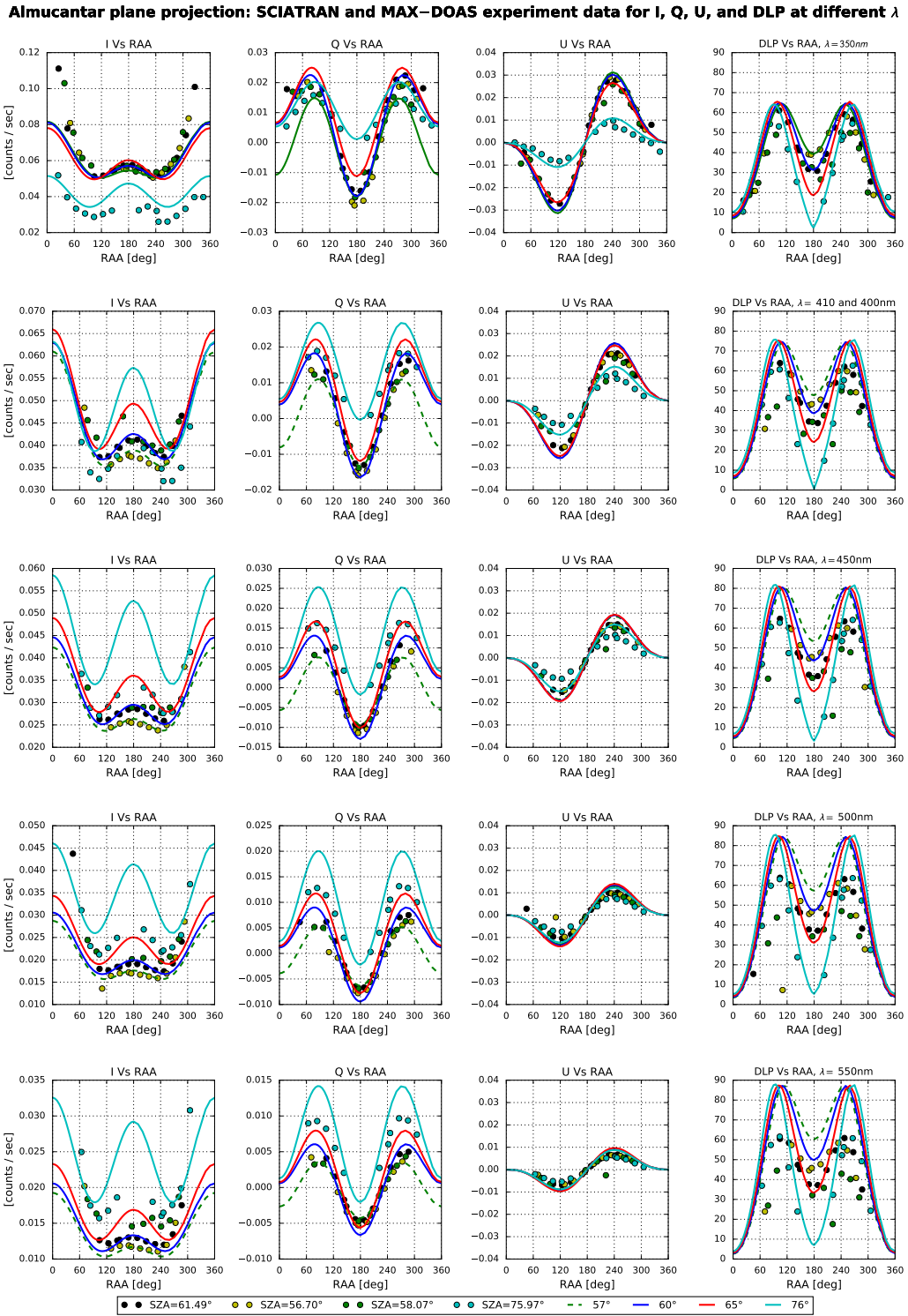
Figure 25: SCIATRAN polarisation simulation and MAX-DOAS experiment: *I, Q, U, DLP* and wavelength dependency for the almucantar plane projection.

6.12 MAX-DOAS experiment: solar principal plane projection vs Line of sight (LOS) in the UV

For the solar principal plane projection, the measurements were performed by pointing the telescope at different SZA with a constant relative azimuth angles as it illustrated in Figure 26. The solid red line denotes the solar plane and the dash red lines corresponds to the points were the data are collected.
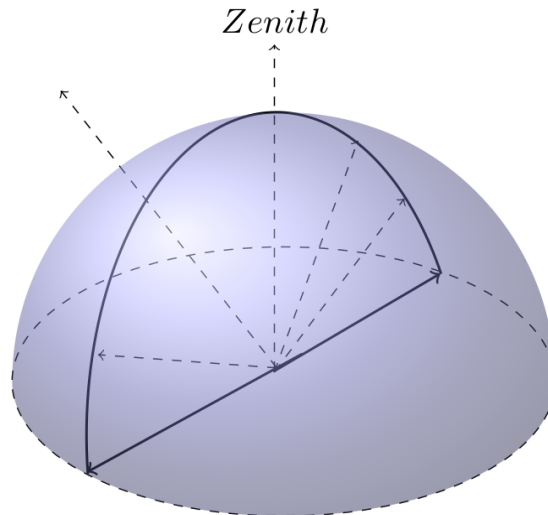
Figure 26: Solar principal plane projection geometry used for the MAX-DOAS measurements

The experimental measurements for the principal plane projection are given in Figure 27. There, all the Stokes components I, Q, U and DLP can be seen. To obtain the figure, the process was quite similar to the production of Figure 19. The first row in Figure 21 shows the experimental data as how they were collected. Through the use of the scale factor $1/(3.65 \times 10^5)$, the experimental measurements were rescaled, as is shown in the second row of the Figure 27. After that, some of the data were removed in accordance to the pictures displayed in the Appendix. The pictures were taken by the instrument at the times of measurements.

Some of the pictures (from the Appendix) showed cases where the DOAS instrument was pointing towards the wall of Naturwissenschaften1 (NW1) building (terrace) or directly to the Sun. These data were removed and the final plot for all the Stokes parameters and the degree of linear polarisation is given in the third row of Figure 27. Additionally, in the fourth row of Figure 27, the SCIATRAN simulation for 350nm in the principal plane at SZA equal to 60° is shown. Finally, in order to get a comparison and to test the accuracy and similarity between the experimental and the simulation data, the fifth row of Figure 27 displays the good relation between both types of data.

Principal plane projection: SCIATRAN polarisation simulation and MAX-DOAS experiment for $\lambda = 350nm$ **and solar zenith angle of 75° and 73.43°**
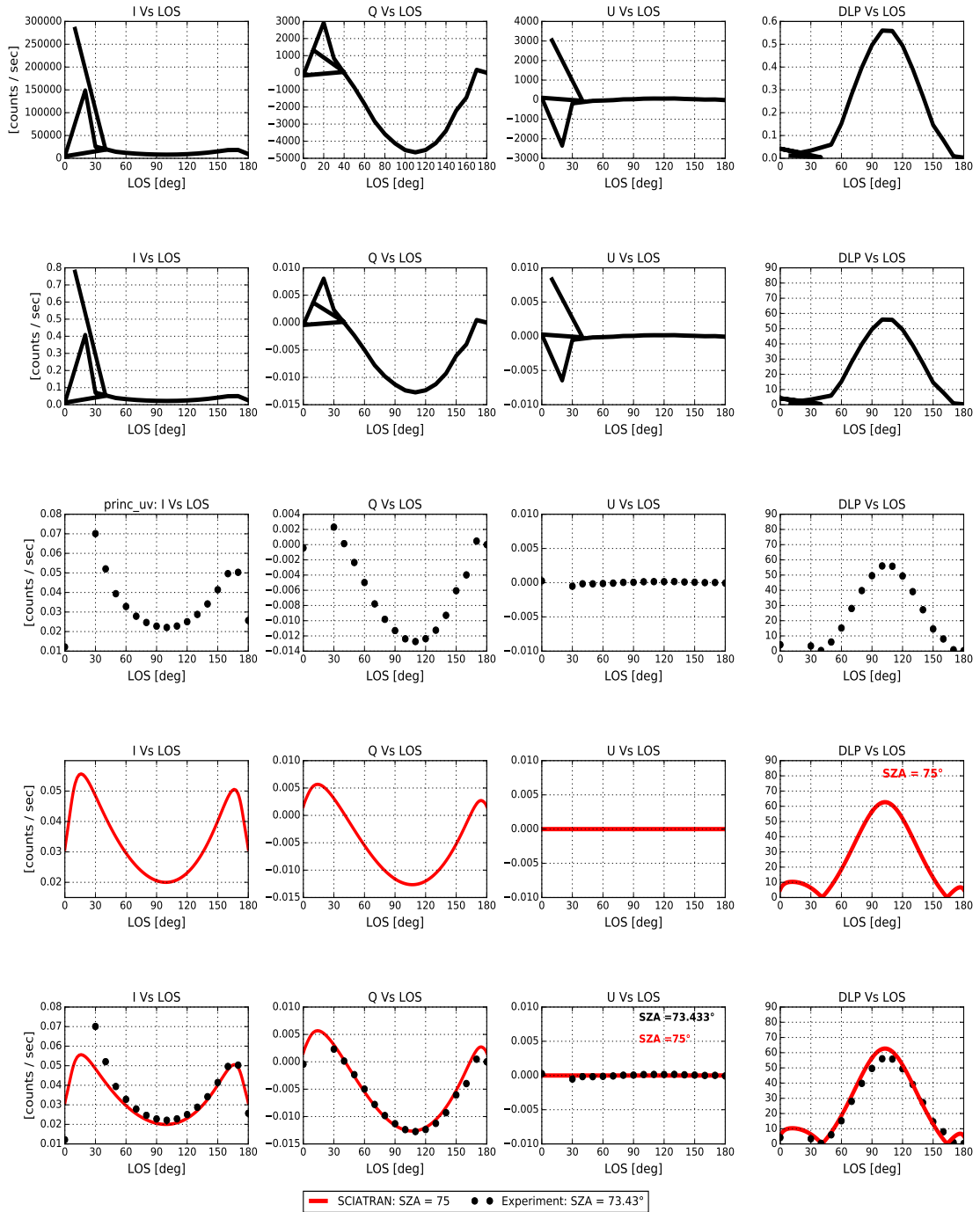
**Figure** 27: Experimental data values of the day 01/10/2017 for the solar principal plane projection at 73.433° SZA (dots) and 75° SZA (red line) for the SCIATRAN polarisation simulation. Both cases for a wavelength of 350nm

By the same procedure as done in Figure 27, for the other data measurements and for the SCIATRAN simulation for the principal solar plane, Figure 28 was created. The Stokes components and the *DLP* are represented by points and solid lines. The dotted lines represent the experimental data after removing the bad data due to the direction of the measurements during the experiment. At some cases the instrument was getting data from the wall of the NW1 (Bremen university) building, and therefore some data were removed.

The new running SCIATRAN simulation for the principal solar plane was performed in order to see how good the experimental data and the simulation with a similar SZA fit were, as is illustrated in the different rows of Figure 28. In general, there is an acceptable agreement between the experimental modified data and the simulated data. The points follow the shape of the lines for the Stokes components and the *DLP*. The maximum of the degree of linear polarisation was slightly higher than 60% for all SZA in the simulated and the experimental data. With 10%, the scattered light was hardly polarized between 0° and 45°(LOS), after that the light is strongly polarized between 45° and 175° (LOS), reaching the maximum value between 100° and 120° (LOS), in accordance to the SZA.

6.13 SCIATRAN polarisation simulations and MAX-DOAS experiment: solar principal plane vs LOS for different SZA in the UV

Regarding the Stokes parameters for the solar principal plane, almost all of them show good agreement between the MAX-DOAS measurements and the SCIATRAN simulated data for a wavelength of 350nm (the other cases will explained in the next section) and for different SZA, as is shown in Figure 28. A particular case is observed for the SZA equivalent to 57.254° and 63.305° in the *I* Stokes graphic. Some of the points reach values higher than 0.10 in the y-axis and they do not follow the profile of the simulated data. The *Q* and *U* Stokes parameters from the experiment, as well as the *DLP*, gave a better fit to the SCIATRAN values, which reaches almost 60% of its maximum value for both scenarios, as well for the MAX-DOAS experiment and the SCIATRAN simulation.
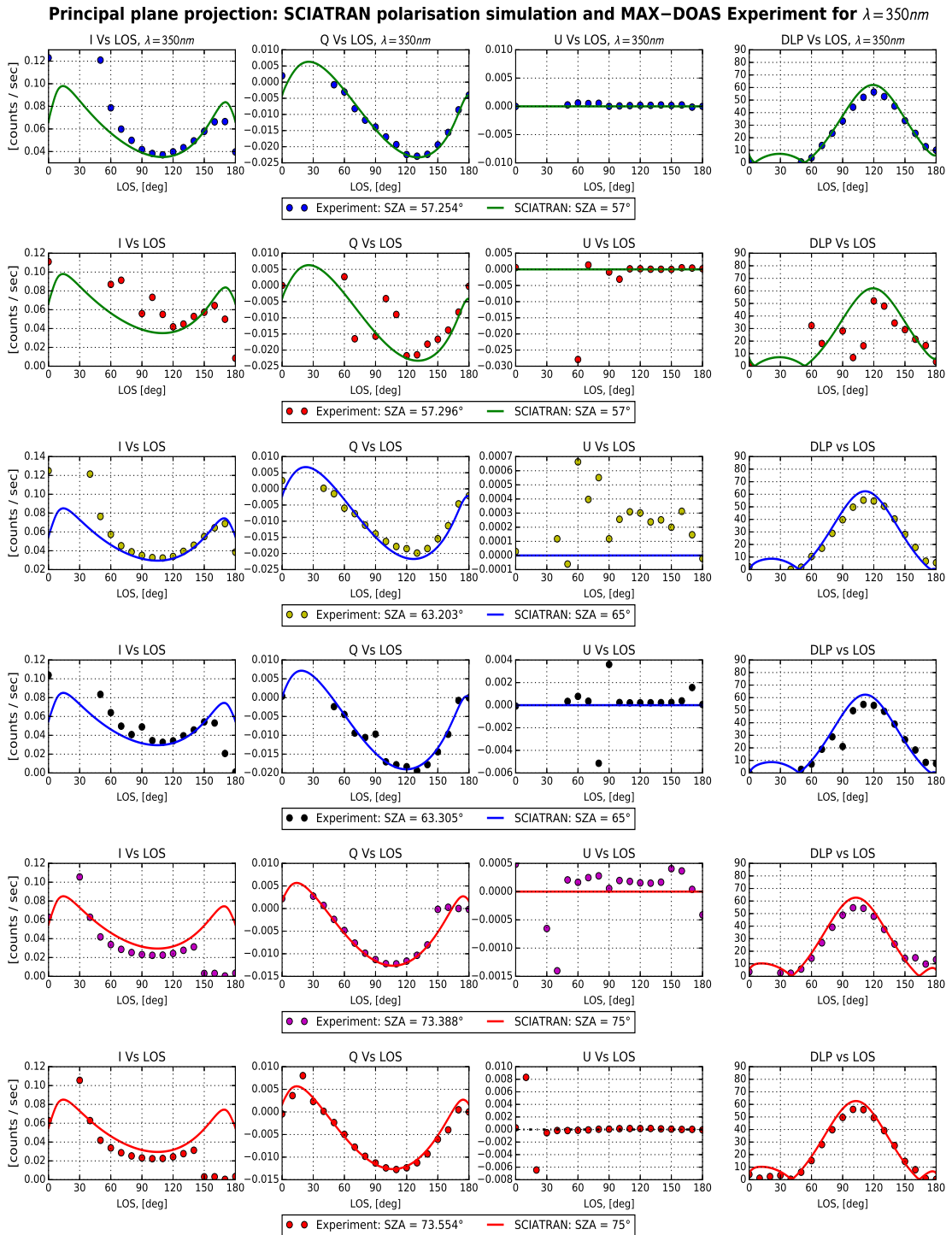
Figure 28: SCIATRAN simulation polarisation and MAX-DOAS experiment for the day 01/10/2017 at different SZA. Simulated data (solid lines) at SZA equal to 57°, 65° and 75°. Dots represent the experimental data.
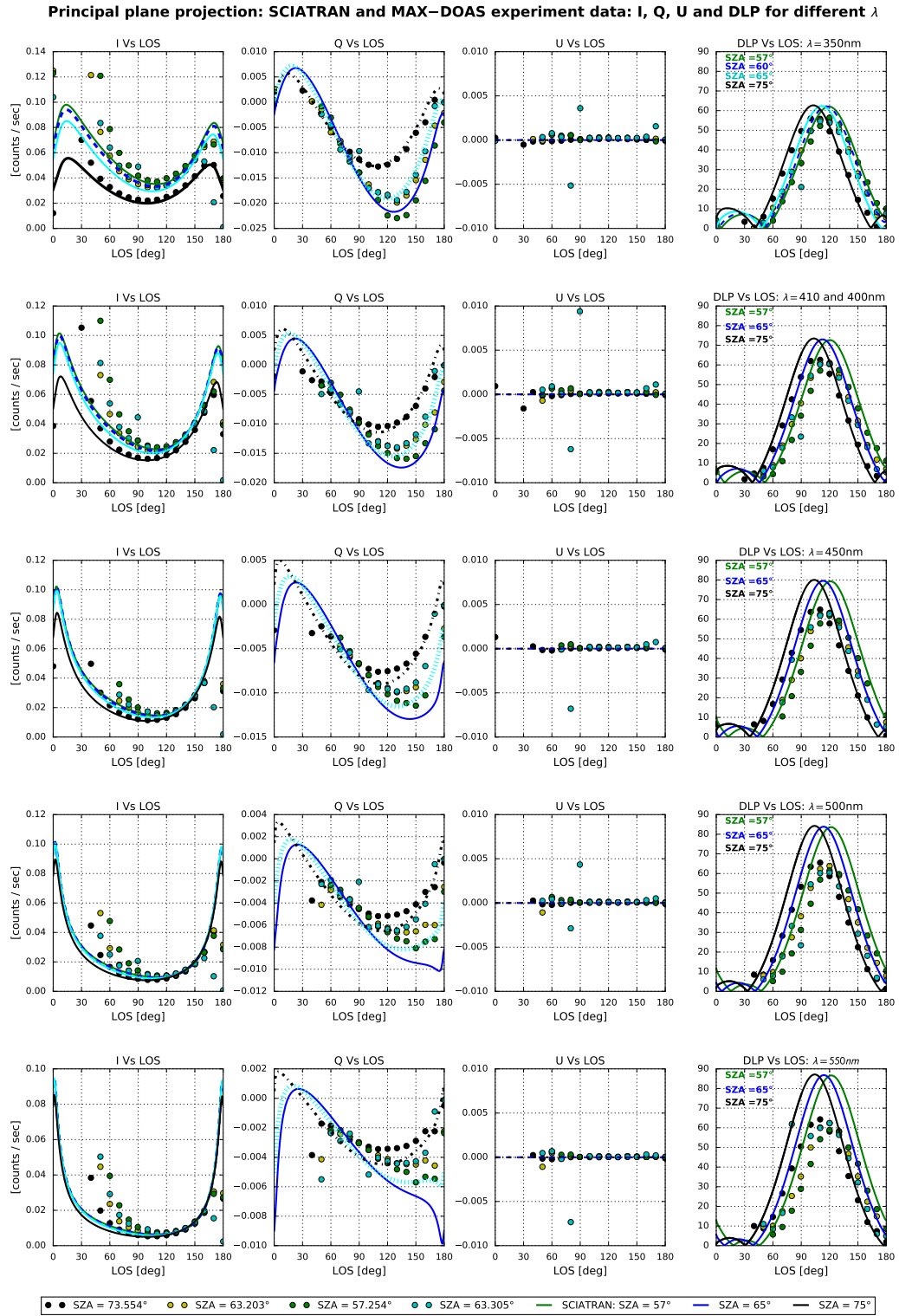
6.14 Dependency on wavelength by SCIATRAN polarisation simulations and MAX-DOAS experiment in solar principal plane projection

As earlier explained, the results for the simulation and the experiment data in the solar principal plane at a wavelength of 350nm showed a positive agreement between the MAX-DOAS polarisation measurements and the SCIATRAN polarisation. However, in order to see how reliable the dependency on wavelength for the Stokes components and DLP can be for the same experimental geometry, the wavelength dependency was studied for five range values: 350nm, 400nm, 450nm, 500 and 550nm for SCIATRAN. The same wavelength ranges were used for the experiment, with the exception of 400nm; instead a wavelength of 410nm was used.

The general variation for the Stokes parameters I, Q, U and the DLP can be seen in Figure 29. Only, for the case of λ equivalent to 350nm, the fit between the MAX-DOAS experiment and the SCIATRAN simulation was reliable. For the other wavelength ranges, the experimental data were far from the simulated data profiles, which can be explained by the increase of wavelength, i.e, at larger λ the experimental data for the Stokes components became higher than the simulated data. The DLP was almost the same value above 60% for all wavelengths from the experimental measurements.

In contradiction to what was observed for SCIATRAN, the DLP was increasing when the wavelengths reached the maximum value of the experimental measurement range, which resulted in a similar behavior as found for the aerosol simulations, as shown in the Figures 19 and 20. Therefore, the observed unfit between the solar principal plane projection of the MAX-DOAS measurements and the SCIATRAN polarisation simulations is due to the presence of aerosols, but can also be related with the scale factor used for the other different wavelengths experimental values.

Figure 29: SCIATRAN polarisation simulation and MAX-DOAS experiment: *I, Q, U, DLP* and wavelength dependency for the solar principal plane projection.

6.15   Polarisation and Wavelength variation

In order to see how the degree of polarisation changes with wavelength, the measurements which had the largest values of *DLP* for a given LOS and RAA in the UV and visible spectrum were selected, as is shown in Figure 30. For as well the UV as the visible spectrum, suitable wavelength *ranges* instead of a specific wavelength were found. For the UV region, an increase of *DLP* is observed, similar to the case of the SCIATRAN simulation for a Rayleigh atmosphere, where it was noticed that the *DLP* also increases when the wavelength becomes larger due to the effect of less multi-scattering in the atmosphere.

In the UV region, an increase in the *DLP* was observed below the 320nm range, probably because of increasing ozone absorption which reduces the probability of multiple scattering. A lot of fine spectral structure can be seen in the *DLP*, reflecting the Fraunhoffer lines in the solar spectrum, which is due to the filling in by unpolarized Raman scattering (Aben et al., 1999). The details of the dependency of *DLP* on wavelength depend on the spectral resolution of the MAX-DOAS instrument as well as on the type and amount of aerosols in the atmosphere. Furthermore, some external conditions are also of importance and influence the time needed to perform the measurements, wherefore the changing character of the atmospheric composition and the solar position should be considered.

To continue with the research on polarisation in the atmosphere, and to continue with the validation of SCIATRAN, it is suggested that new SCIATRAN simulations should try to include the Raman scattering, and should try to be compared to MAX-DOAS experimental measurements.
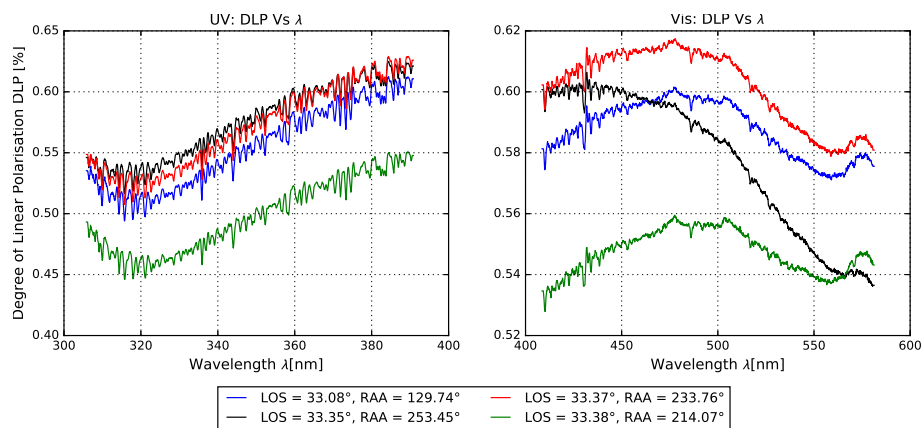
Figure 30: Variation of the *DLP* against the wavelength range for the MAX-DOAS experiment on 01/10/2017 at different LOS and RAA.

7 Discussion

The goal of this thesis was to assemble a suitable optical set-up to enable the MAX-DOAS instrument to perform polarisation sensitive measurements and to take a series of measurements on clear days. An additional objective was to run SCIA-TRAN for the appropriate scenarios, and compare them with the measurements. In order to achieve the first objective, the Bremen MAX-DOAS instrument was adapted with a Glan-Thompson polarizer, and was tested to see whether the polarizer as well as the computer program functioned correctly, and to assess if the collected signal from the sky light made sense. For a possible new experiment with an instrument similar to MAX-DOAS, it is suggested to increase the size of the set-up (the box) in order to be able to add new elements in a more practical way. A new element can be a lens (fisheye) for the camera to obtain a complete picture of where the measurement is performed

To be able to assess the second aim of the master thesis, polarized measurements of radiance from the sky were performed during three reasonable clear days: 24th of September, 1st and 8th October of 2017 from 7:00 to 16:00, in intervals with an average time of 15 minutes, every hour or during the change of an hour. However, due to clouds and haze at different moments during the measurements, the most suitable collected experimental data are from the 1st October, and are shown in the Figures 23, 24, 25, 27, 28, 29 and in the Appendix figures.

About the third goal of the project, running SCIATRAN for appropriate scenarios, it was achieved first of all with the help of a publication of (Emde et al., 2010), where SCIATRAN polarisation simulations were performed for the following scenarios: a Rayleigh atmosphere, an atmosphere with continental, maritime and urban aerosols and simulations with a variation in some of the given parameters, which were among others: SZA, Azimuth, LOS, AOD, wavelength range, geometrical scenarios, as is shown in the Figures 12-13 and 18-21. For a possible new set of the SCIATRAN simulations, new scenarios can be tested which should use a more expanded dataset on aerosols, or should consider a mixture of different aerosols sources (e.g. continental, maritime and urban), an option which is currently missing in the used version of SCIATRAN for this thesis.

In general, the experimental data are in good agreement with the results obtained in the simulations performed with SCIATRAN for a Rayleigh atmosphere at a wavelength of 350nm. The measured radiances correspond to a range of SZA between 56° and 76° in the almucantar plane projection, and 57° to 73° in the principal solar plane projection, as is shown in Figures 17 and 20. Measurements of radiance (intensity) with SZA lower than 56° are not possible due to the geographical position of Bremen.

The experimental values (in magnitude) for the Stokes components *I, Q, U* and the degree of linear polarisation (*DLP*) show an acceptable agreement with the results from (Emde et al., 2010). The measured radiance needed to be calibrated empirically with a scaling factor to get a better agreement between the measured and the simulated radiances. Several factors were evaluated, but the most consistent result was obtained for a factor of $1/(3.65 \times 10^5)$.

Some data were not included in the comparison, for example if the MAX-DOAS instrument was pointing towards the wall of the NW1 building of the Bremen University (see Appendix), or when clouds were present, or when a signal data was obtained from direct sunlight measurements. Without these considerations, the computed Stokes components and the *DLP* would be away from the the expected magnitude values. Also, the shape of every curve of these variables would be biased and not comparable to the lines in the SCIATRAN simulation.

The SCIATRAN polarisation simulations were performed for two main conditions, first for a Rayleigh atmosphere, which means an atmosphere free of aerosols and clouds. The second scenario, slightly closer to the reality, was a simulation with the presence of aerosols. The simulations have been performed by first trying to reproduce the same results as published by (Emde et al., 2010), as is shown in Figures 13, 16, and 17.

Thus, the first running simulation was performed at SZA of 0°, 10°, 30° and 60° in the polar projection, the solar principal plane projection and the almucantar plane projection, and did show an excellent agreement with the results published by (Emde et al., 2010), and reproduced here by the Figures 12 and 13. Therefore, by SCIATRAN simulation for a Rayleigh atmosphere, it was possible to reproduce the same results achieved by the use of MYSTIC as in the publication of (Emde et al., 2010).

For the second scenario, it was not possible to use the same data set of aerosols (OPAC) as employed by (Emde et al., 2010). Instead, three types of aerosols were employed for the SCIATRAN simulations, namely continental, maritime and urban. For each aerosol condition, independent SCIATRAN simulations have been performed. A mix between the aerosols is not possible in the current version of SCIATRAN. Nevertheless, in comparison to Figure 15, the collected simulated data shown in Figure 16 behaves adequate in reference to the tendency of the different curves at 60° of SZA.

The peak in the intensity appears in all the simulations with the different types of aerosols. In all cases, the maximum was found at a LOS of 30° because the Sun is in that angle position. However, the aerosols, which have a similar behavior for the intensity as well as for the *DLP*, correspond to maritime aerosols (see Figure 18). Thus, in order to see more detailed how the intensity and the *DLP* change over different wavelengths, Figure 19 was created for all the wavelength ranges used for the simulation.

The peak of the intensity was not uniform for all wavelengths, and there is a small fluctuation when the intensity reaches its maximum value, which only happened for the largest wavelength. Furthermore, for small wavelengths, the intensity was also smaller. A similar situation can be observed in the *DLP*, for shorter wavelengths: the *DLP* was lower and achieved its maximum value at 60° for 550nm, which represents a strong polarisation of sky-light.

As a second comparison to the study of (Emde et al., 2010), a simulation including aerosols was performed. For this case, urban aerosols were selected to be able to see the variation in the intensity and the *DLP* when the AOD was increasing, as shown in Figure 20. The main results show a slight decrease in the *DLP* for every 10% of unit, when the AOD increased by 0.1[1/Km], 0.25[1/Km], 0.5[1/Km] and 1.0[1/Km]. The intensity however showed a different behavior, with two maximum values for AOD of 0.25[1/Km] and 0.5[1/Km].

All the results from Figure 20 were generated by the use of a wavelength of 377nm for the wavelength coefficient extinction. However, as the dependency of the intensity and *DLP* were already studied in function of wavelength and AOD, a new attempt to see how close the results were in respect to Figure 17 was produced using urban aerosols with a constant AOD. For this case, a variation in the wavelength for the coefficient extinction was tested for 377nm, 400nm, 488nm, 515nm and 550nm, as is shown in Figure 21.

From Figure 21, the observed *DLP* and intensity behave quite different from the previous results when several values of AOD were used. What can be observed in Figure 21 is a small change in the value of *DLP*, which was around 40% for all the tested cases. Furthermore, the intensity was decreasing when the wavelength for the extinction coefficient was increasing. So, Figure 21 displays acceptable similarities in accordance to the profiles of I and *DLP* which are shown in Figure 17.

For a comparison with the experimental data, SCIATRAN was run for a new SZA at values of 57°, 65°, 75° and 76°, as is shown in Figures 24 and 26. Figure 24 presents a good agreement for the measurements for all the Stokes parameters and DLP in the almucantar plane projection and the SCIATRAN simulations for a wavelength of 350nm. Only the I Stokes parameter showed small differences for a SZA equal to 76° for as well the simulated data as the experimental measurements. The experimental data of I were not so close to the simulated data, as they were for the other Stokes components.

This variation for the I Stokes component results in a lower value for the experimental data relative to the simulated data when smaller wavelengths are considered. This lack of fit cannot only be caused by the scale factor, but is more likely caused by external factors such as clouds, aerosols, haze, cloud drops, or the presence of a disturbance (such as the terrace of the NW1 building).

In Figure 23, the simulated and experimental data for the almucantar plane projection show a good fit for the Stokes components. However, for some experimental data points, the I Stokes parameter shows values far from the simulated data. Some of the points get higher values around 30° in the LOS. This can be an indicator for the effect of aerosols in polarisation, as was shown in the Figures 18, 19, 20 and 21 where SCIATRAN simulations for aerosols scenarios are presented. Thus, for a better fit for the experimental data as collected on the 1st of October, it is suggested to use a simulation which takes aerosols into account instead of a simulation for a Rayleigh atmosphere.

In conclusion, a positive fit was found between the MAX-DOAS measurements and the SCIATRAN polarisation simulation for the almucantar plane projection at 350nm. The dependency on wavelength for this scenario was also studied for 400nm, 450nm, 500nm and 550nm from SCIATRAN data values and for the same range for experimental data, with a small difference where 410nm was used instead of 400nm. Thus, the main differences show a relative decrease of the SCIATRAN Stokes components in comparison with the MAX-DOAS Stokes parameters, which in fact are increasing less when the wavelength for the computer model and the experiment are increasing.

All the Stokes parameters from the MAX-DOAS measurements follow the same shape as the I, Q, and U estimated from SCIATRAN, however, their order of magnitude is higher than the expected values from the simulation. Moreover, the situation for the DLP showed a different trend. DLP by SCIATRAN became higher at every increment of the wavelength reaching a maximum value of 80%, and therefore serves as a good indicator of how much light was polarized. However, in reality, the DLP was lower than that: 60% was the maximum value obtained by the use of MAX-DOAS instrument, which was almost the same value when the wavelength was increased.

For the case of the solar principal plane at 350nm the SCIATRAN and the MAX-DOAS measurements displayed both reliable behavior. However, for the other wavelengths, the Stokes components showed a behavior more related to the profile of *I, Q, U*, and the *DPL* showed a closer behavior to an atmospherere with aerosols at different SZA. Furthermore, the experimental *DLP* was lower than the simulated one even when the SZA angles for both scenarios where almost the same. Thus, not only aerosols, weather conditions, or objects with a significant size affecting the received signal, as was experienced for example by the wall of the NW1 building, can be the cause of the dissimilarities among the Stokes components and the *DLP*.

By studying the degree of polarisation and its dependency in respect to the wavelength range given by the MAX-DOAS measurements, some differences in the behavior of the *DLP* in the UV and in the visible regions were found. The variation of *DLP* was observed for the UV and visible spectrum, showing in general an increase in the *DLP* in the UV region when λ is increasing and because the multiple scattering in that region is reduced. In the case of the opposite scenario, when the *DLP* decreases for larger wavelengths, such as around 475nm, it starts to get lower values. In both cases the reduction of DLP can also be due to reflection from the ground.

8   Summary and Conclusion

The IUP-Bremen MAX-DOAS instrument was equipped with a computer controlled UV Glas-Thompson polarizer in the telescope, and several weeks of automated measurements were performed. Polarisation simulations for several scenarios were done with the help of the SCIATRAN software. The first simulations were performed in order to reproduce part of the results which were obtained by (Emde et al., 2010). SCIATRAN simulations were in a good agreement with the simulations performed by (Emde et al., 2010) with the program MYSTIC, indicating a proper choice of SCIATRAN parameters.

The second set of simulations were performed to compare and validate the obtained experimental data. For the validation of the data, the scale factor $1/(3.65 \times 10^5)$ gave a good approximation for the experimental measurements and the simulated data, particularly for the almucantar plane projection. Therefore, the MAX-DOAS instrument worked very well for the validation and the application of SCIATRAN polarisation simulation and ground-based measurements.

For the future, more MAX-DOAS measurements should be performed to extend the data for smaller solar zenith angles and other aerosol conditions. This could be done by taking measurements through summer. Furthermore, for the case of aerosols simulations, it would be good to test a mix of aerosols types, such as urban, maritime or continental, to be able to obtain a better similarity between the modeled data and the acquired measurements.

Apart from the suggestion to perform MAX-DOAS measurements for different scenarios, it could also be suitable to incorporate more data (amount) and include more atmospheric variables. This will allow the study of polarisation in more detail, which can be used to enhance the retrieval information of trace gases in the atmosphere.

9 Appendix

A) Example of pictures used to identify experimental data where the view was blocked.

Figure 31: Example pictures taken with the telescope video camera during the experiment measurements and used to identify cloudy or blocked data.

B) MAX-DOAS instrument on the terrace of Bremen University NW1 Building. (Wall disturbance over the measured data)

Figure 32: Wall interference of the DOAS measurements.

References

Aben, I., Helderman, F., Stam, D. M., and Stammes, P.: Spectral Fine-Structure in the Polarisation of Skylight, Geophysical Research Letters, 26, 591–594, doi: 10.1029/1999GL900025, 1999.

Band, Y. B.: Light and Matter: Electromagnetism, Optics, Spectroscopy and Lasers, John Wiley, Chichester, 2006.

Bohren, C. F. and Clothiaux, E. E.: Fundamentals of Atmospheric Radiation: An Introduction with 400 Problems, Wiley-VCH, Weinheim, 2006.

Borrell, P., Borrell, P. M., Burrows, J. P., and Platt, U., eds.: Sounding the Troposphere from Space: A New Era for Atmospheric Chemistry, Springer, 2012.

Burrows, J. P., Weber, M., Buchwitz, M., Rozanov, V., Ladstätter-Weißenmayer, A., Richter, A., DeBeek, R., Hoogen, R., Bramstedt, K., Eichmann, K.-U., Eisinger, M., and Perner, D.: The Global Ozone Monitoring Experiment (GOME): Mission Concept and First Scientific Results, Journal of the Atmospheric Sciences, 56, 151–175, doi:10.1175/1520-0469(1999)056⟨0151:TGOMEG⟩2.0.CO;2, 1999.

Carlson, D., Donohoue, D., Platt, U., and Simpson, W. R.: A Low Power Automated MAX-DOAS Instrument for the Arctic and Other Remote Unmanned Locations, Atmos. Meas. Tech., 3, 429–439, doi:10.5194/amt-3-429-2010, 2010.

Chandrasekhar, S. and Elbert, D. D.: The Illumination and Polarization of the Sunlit Sky on Rayleigh Scattering, Transactions of the American Philosophical Society, 44, 643–728, doi:10.2307/1005777, 1954.

Curran, P. J.: Polarized Visible Light as an Aid to Vegetation Classification, Remote Sensing of Environment, 12, 491–499, doi:10.1016/0034-4257(82)90023-2, 1982.

Emde, C., Buras, R., Mayer, B., and Blumthaler, M.: The Impact of Aerosols on Polarized Sky Radiance: Model Development, Validation, and Applications, Atmos. Chem. Phys., 10, 383–396, doi:10.5194/acp-10-383-2010, 2010.

Emde, C., Barlakas, V., Cornet, C., Evans, F., Korkin, S., Ota, Y., Labonnote, L. C., Lyapustin, A., Macke, A., Mayer, B., and Wendisch, M.: IPRT Polarized Radiative Transfer Model Intercomparison Project – Phase A, Journal of Quantitative Spectroscopy and Radiative Transfer, 164, 8–36, doi:10.1016/j.jqsrt.2015.05.007, 2015.

Hansen, J. E. and Hovenier, J. W.: Interpretation of the Polarization of Venus, Journal of the Atmospheric Sciences, 31, 1137–1160, doi:10.1175/1520-0469(1974)031⟨1137:IOTPOV⟩2.0.CO;2, 1974.

Hasekamp, O. P. and Landgraf, J.: Tropospheric Ozone Information from Satellite-Based Polarization Measurements, Journal of Geophysical Research: Atmospheres, 107, 4326, doi:10.1029/2001JD001346, 2002.

Horváth, G. and Varjú, D.: Polarized Light in Animal Vision: Polarization Patterns in Nature, Springer, Berlin ; New York, 2004.

Jackson, J. D.: Classical Electrodynamics, Wiley, New York, 2 edn., 1975.

Jonasz, M. and Fournier, G.: Light Scattering by Particles in Water Theoretical and Experimental Foundations, Elsevier Ltd, 1st edn., 2007.

Kokhanovsky, A. A.: Light Scattering Media Optics Problems and Solutions, Springer, 3 edn., 2004.

Kokhanovsky, A. A.: Aerosol Optics: Light Absorption and Scattering by Particles in the Atmosphere, Springer-Praxis books in environmental sciences, Springer ; Praxis, Berlin ; New York : Chichester, UK, 2008.

Können, G. P.: Skylight Polarization during a Total Solar Eclipse: A Quantitative Model, 4, 601–608, doi:10.1364/JOSAA.4.000601, 1987.

Können, G. P. and Beerling, G. A.: Polarized Light in Nature, Cambridge Univ. Press, Cambridge, 1985.

Kozlov, A.I., Ligthart, L.P., and Logvin, A.I.: Mathematical and Physical Modelling of Microwave Scattering and Polarimetric Remote Sensing., Springer, 2004.

Kreuter, A., Emde, C., and Blumthaler, M.: Measuring the Influence of Aerosols and Albedo on Sky Polarization, Atmospheric Research, 98, 363–367, doi:10.1016/2010.07.010, 2010.

Landgraf, J., Hasekamp, O. P., van Deelen, R., and Aben, I.: Rotational Raman Scattering of Polarized Light in the Earth Atmosphere: A Vector Radiative Transfer Model Using the Radiative Transfer Perturbation Theory Approach, Journal of Quantitative Spectroscopy and Radiative Transfer, 87, 399–433, doi:10.1016/j.jqsrt.2004.03.013, 2004.

Liou, K. N.: An Introduction to Atmospheric Radiation, Volume 84, Second Edition, Academic Press, Amsterdam ; Boston, 2nd edn., 2002.

Martin, S.: An Introduction to Ocean Remote Sensing, Cambridge University Press, Cambridge, UK ; New York, 1 edition edn., 2004.

Platt, U. and Stutz, J.: Differential Optical Absorption Spectroscopy: Principles and Applications, Springer, Berlin, 2008.

Rozanov, V. V., Rozanov, A. V., Kokhanovsky, A. A., and Burrows, J. P.: Radiative Transfer through Terrestrial Atmosphere and Ocean: Software Package SCIATRAN, Elsevier Ltd, 2014.

Salby, M. L. and Dmowska, R.: Fundamentals of Atmospheric Physics, Volume 61, Academic Press, San Diego, 1st edn., 1996.

Sekera, Z.: Light Scattering in the Atmosphere and the Polarization of Sky Light*, 47, 484–490, doi:10.1364/47.000484, 1957.

Stamnes, K. and Stamnes, J. J.: Radiative Transfer in Coupled Environmental Systems: An Introduction to Forward and Inverse Modeling, Wiley-VCH, Weinheim, 1st edn., 2015.

Tilstra, L. G., Lang, R., Munro, R., Aben, I., and Stammes, P.: Contiguous Polarisation Spectra of the Earth from 300 to 850nm Measured by GOME-2 Onboard MetOp-A, Atmospheric Measurement Techniques, 7, 2047–2059, doi:10.5194/amt-7-2047-2014, 2014.

Tousey, R. and Hulburt, E. O.: Brightness and Polarization of the Daylight Sky at Various Altitudes above Sea Level, 37, 78–92, doi:doi.org/10.1364/JOSA.37.000078, 1947.

Vountas, M., Rozanov, V. V., and Burrows, J. P.: Ring Effect: Impact of Rotational Raman Scattering on Radiative Transfer in Earth's Atmosphere, Journal of Quantitative Spectroscopy and Radiative Transfer, 60, 943–961, doi:10.1016/S0022-4073(97)00186-6, 1998.

Vountas, M., Richter, A., Wittrock, F., and Burrows, J. P.: Inelastic Scattering in Ocean Water and Its Impact on Trace Gas Retrievals from Satellite Data, Atmos. Chem. Phys., 3, 1365–1375, doi:10.5194/acp-3-1365-2003, 2003.

Wagner, T., Dix, B., v. Friedeburg, C., Frieß, U., Sanghavi, S., Sinreich, R., and Platt, U.: MAX-DOAS O_4 Measurements: A New Technique to Derive Information on Atmospheric Aerosols-Principles and Information Content: MAX-DOAS O_4 Measurements of Aerosols, Journal of Geophysical Research: Atmospheres, 109, doi:10.1029/2004JD004904, 2004.

Wallace, J. M. and Hobbs, P. V.: Atmospheric Science an Introductory Survey In:International Geophysics Series ; 92, Elsevier Ltd, 2 edn., 2006.

Declaration of Authorship

I hereby confirm that I have authored this Master's thesis independently and without use of others than the indicated sources. All passages which are literally or in general matter taken out of publications or other sources are marked as such.

Bremen, December 29, 2017.

Andrés.

.